

國立交通大學

機械工程學系

碩士論文

應用適應控制之 H 型壓電陀螺儀的設計與控制



**Design and Control of the H-type Piezoelectric
Gyroscope via Adaptive Control Strategies**

研究生：黃建評

指導教授：陳宗麟 博士

中華民國九十四年七月

應用適應控制之 H 型壓電陀螺儀的設計與控制

**Design and Control of the H-type Piezoelectric Gyroscope
via Adaptive Control Strategies**

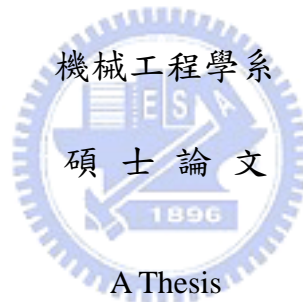
研究生：黃建評

Student: Chien-Ping Huang

指導教授：陳宗麟 博士

Advisor: Dr. Tony Chen

國立交通大學



Submitted to Department of Mechanical Engineering
College of Engineering
National Chiao Tung University
in partial Fulfillment of the Requirement
for the Degree of
Master of Science
in
Mechanical Engineering
July 2005
Hsinchu, Taiwan, Republic of China

中華民國九十四年七月

應用適應控制之 H 型壓電陀螺儀的設計與控制

研究生：黃建評

指導教授：陳宗麟博士

國立交通大學機械工程學系

摘要



近十年來，微機電系統(MEMS)感測器的發展逐漸受到矚目。受惠於現今積體電路製造技術，微機電系統通常具有小尺寸和輕量化等微型設計的優點。本文主要目的在設計一種可利用現今製造技術生產之微機電型態的壓電式陀螺儀。根據現有之 H 型陀螺儀所具有的低電耦合與低機械耦合效應之優點，本文提出了新式 H 型壓電陀螺儀並且探討其型態的概念設計和相關的耦合效應。另外，根據壓電陀螺儀的操作原則，再搭配上適應性控制的演算法則，將可鑑別且消除在製程上所產生的校正偏差和機電耦合效應。

Design and Control of the H-type Piezoelectric Gyroscope via Adaptive Control Strategies

Student: Chien-Ping Huang

Advisor: Dr. Tony Chen

Department of Mechanical Engineering
National Chiao Tung University

ABSTRACT

Microelectromechanical systems (MEMS) sensors have received lots of attention over the last decade. With the virtue from present IC fabrication techniques, they generally have the advantages of being lightweight, being small in size, etc. In this thesis, we designed a MEMS PZT gyroscope based on the in-situ fabrication process. The conceptual design and the coupling effects in our proposed gyroscope are presented in this report. This design is based on the existing H-type gyroscope, which has the advantage of reducing electrostatic and mechanical coupling effects existed in between the driving and detecting axes. The fabrication errors and the electromechanical coupling were identified and null out by the adaptive algorithms along the operation of this gyroscope.

ACKNOWLEDGEMENT

本論文得以順利完成，首先要感謝我的指導教授陳宗麟老師的指導，在老師嚴謹的治學帶領下，總是能周詳地考慮所面臨的問題，在作者產生疑惑時，一針見血地點明癥結點，並且加以指導、糾正；兩年的光陰，作者受益良多，在此致上最誠摯的感謝。

同時感謝口試委員呂宗熙教授、蘇育全教授對本論文給予的指導與建議，以及固控組諸位老師，對於作者課業上的指導與關懷。

感謝實驗室學長紀建宇對作者研究上的指教，學弟許齡元、林志柏、高忠福及同學陳奕龍、邱仕釗、郭威廷的相互砥礪，使作者的課業及研究工作得以順利進行，在此一併致謝。

另外感謝好友汪詠欽、楊文嘉、鄭智仁、林珮綺、顏得修、張孟瑜的支持與鼓勵，使作者的研究生活得以順利進行。

最後謹將本論文獻給最親愛的父母親，感謝他們多年來付出的辛勞，在他們的細心呵護下，作者才有今天小小的成果，希望能與他們分享今日的喜悅；親友的支持與鼓勵，使作者在無後顧之憂下完成學業，謹此獻上最誠摯的謝意。

TABLE OF CONTENTS

摘要	II
ABSTRACT	III
ACKNOWLEDGEMENT	IV
TABLE OF CONTENTS.....	V
LIST OF TABLE.....	VIII
LIST OF FIGURE	IX
Chapter 1 Introduction	1
1.1 Gyroscope	1
1.2 Vibratory Gyroscope	2
1.3 Survey of H-Type Piezoelectric Gyroscopes	2
1.3.1 Complicated Couplings of Piezoelectric Gyroscopes.....	3
1.3.2 Suppression of Unnecessary Couplings.....	4
1.4 Survey of Adaptive Control Methods for the gyroscope	6
1.5 Outline of the Thesis	7
Chapter 2 Theory of Piezoelectric Material	9

2.1 Piezoelectric Material	9
2.2 Piezoelectric Constitutive Equations	10
Chapter 3 Preliminary Design of Piezoelectric Gyroscope .	14
3.1 Design of Piezoelectric Gyroscope Configuration	14
3.1.1 Case I: The Y-type piezoelectric gyroscopes	14
3.1.2 Case II: The H-type piezoelectric gyroscopes	15
3.2 Electrostatic Coupling Analysis and Reduction	16
3.3 Dynamics for the Designed Gyroscope	17
3.3.1 Dynamic Motion of the Designed Gyroscope	17
3.3.2 Frequency Response & Approximate 2 nd Order Model.....	18
3.3.3 Modeling the Electromechanical Coupling	20
3.3.4 Convergence Analysis of Result by ANSYS	22
Chapter 4 Adaptive Control of Piezoelectric Gyroscope.....	23
4.1 Adaptive Control Strategies	23
4.2 Estimation of Noise.....	26
4.3 Simulation Results and Discussion.....	28
Chapter 5 CONCLUSION AND FUTRE WORKS	32
5.1 Conclusion	32
5.2 Future Works.....	32

APPENDIX I..... 34

Reference 40



LIST OF TABLE

Table 1 Electromechanical Coupling Coefficients for Driving and Detecting Electrodes (fork type) [2]	43
Table 2 Electromechanical Coupling Coefficients for Symmetrical Electrode [2]	43
Table 3 The properties of the four piezoelectric state variables	44
Table 4 The matrix properties of the different forms	44
Table 5 Compliance Constants of LiTaO_3	45
Table 6 Piezoelectric Strain Constants of LiTaO_3	45
Table 7 Permittivity Strain Constants of LiTaO_3	46
Table 8 Stiffness Constants of LiTaO_3	46
Table 10 Power Spectral Density of Noise	47
Table 11 Parameters of the designed H-gyro	48
Table 12 Parameters of Approximated 2nd Order Model	48
Table 13 Selected Adaptive Control Gains	48
Table 14 Parameters of Different Configurations	49



LIST OF FIGURE

Figure 1.1 Coupling classifications of gyroscope.....	50
Figure 1.2 Conventional fork type piezoelectric gyroscope	50
Figure 1.3 H-type LT piezoelectric gyroscope [2]	51
Figure 2.1 Inertia coordinate of the piezoelectric material	51
Figure 3.1 bending model concept.....	52
Figure 3.2 Bending mode simulation by ANSYS.....	52
Figure 3.3 Displacement vs. frequency of bending mode	53
Figure 3.4 The designed gyroscope (case I)	53
Figure 3.5 Size of the designed gyroscope model	54
Figure 3.6 Configuration of gyroscope model (case II).....	54
Figure 3.7 Modal analysis of the designed model by ANSYS (H mode)	55
Figure 3.8 Modal analysis of the designed model by ANSYS (Y mode)	55
Figure 3.9 Lateral view of the designed model by ANSYS (H mode)	56
Figure 3.10 Lateral view of the designed model by ANSYS (Y mode)	56
Figure 3.11 Schema of equivalent circuit between driving and detection electrodes	57
Figure 3.12 Configuration of the designed model by ANSYS	57
Figure 3.13 Frequency response with intermediate isolation	58
Figure 3.14 Frequency response without any intermediate limit.....	58
Figure 3.15 Frequency response with intermediate planar electrode GND.	59
Figure 3.16 Relative displacements of the designed model (Y mode)	59
Figure 3.17 Relative displacements of the designed model (H mode)	60
Figure 3.18 Curve fitting of frequency response (H mode).....	60
Figure 3.19 Curve fitting of frequency response (Y mode).....	61
Figure 3.20 Convergence analysis (H mode).....	61
Figure 3.21 Convergence analysis (fork mode).....	62
Figure 4.1 Trajectories of x and y axes (a) tracking signal of x axis. (b) tracking signals of y axis.....	62
Figure 4.2 (a) tracking error of x axis. (b) tracking error of y axis.....	63
Figure 4.3 Estimations of damping terms. (a) estimation of D_{xx} . (b) estimation of D_{xy} . (c) estimation of D_{yy}	63
Figure 4.4 Estimations of R terms. (a) estimation of R_{xx} . (b) estimation of R_{xy} . (c) estimation of R_{yy}	64
Figure 4.5 Estimation of angular velocity.....	64
Figure 4.6 Control input of x axis.....	65

Figure 4.7 Control input of y axis.....65
Figure 5.1 Planar electrode design of H-gyro.....66



Chapter 1

Introduction

1.1 Gyroscope

Gyroscopes have been extensively used to measure the angular velocity in many applications in our daily lives such as vehicle navigation, vehicle rollover stability, digital camera image stabilization, and even in advanced military applications like aircrafts and satellites. In recent years, due to the regular need for better sensitivity, the development of gyroscopes are still in process and still attract attentions from the researchers in various fields.

The first appearance of gyroscope can be tracked to the year 1852, Leon Foucault (1819-1868), a 19th-century French experimental physicist, who used the “gyroscope” apparatus to investigate the rotation of the earth. After that, along with the technologies advances, there are multiple variances in the development of gyroscopes. Due to the surge of virtual reality, and other applications as well, the development of gyroscope moves towards sensitive, reliable and miniature size for mass production.

According to their working principles, gyroscopes can be roughly classified to mechanical gyroscopes (rotor gyroscopes, vibratory gyroscopes and etc.) and optical gyroscopes (fiber gyros and laser gyros etc.). They all have their pros and cons and been utilized in various applications. MEMS technology, due to the advantages of being small in size and cheap in fabrication, has received more and more attention in specific applications.

1.2 Vibratory Gyroscope

Most of the mechanical gyroscopes can be classified to the vibratory gyroscopes and they detect the angular rate based on the principles of Coriolis force. The basic idea of the vibratory gyroscope is that when the mass is oscillating along one axis (driving axis) and experiencing the angular velocity simultaneously, the Coriolis force will produce a force along the axis (detecting axis) that is orthogonal to its original oscillating axis. Furthermore, the amplitude of the detecting axis is proportional to the applied angular velocity.

1.3 Survey of H-Type Piezoelectric Gyroscopes

Various vibratory gyroscopes have been proposed these days; they include ring gyroscopes, beam gyroscopes, shell gyroscopes, and fork gyroscopes etc. Fork gyroscopes and its related version of H-type gyroscopes are both the important designs of vibratory gyroscope, and H-type gyroscopes are improved configuration since they can reduce the coupling effects between driving and detecting axis. Wakatsuki [1, 2] proposed the prototype of H-Type LiTaO_3 Piezoelectric Gyroscope in 1997 and claimed that it had a better ability to suppress the leakage couplings than that of the fork gyroscope. Moreover, the H-type vibratory gyroscope using LiTaO_3 single crystal has large electromechanical coupling coefficients, which can sharply suppress the “leakage” output. He also suggested that using a transducer attached to the driving axis to monitor and compensate the temperature drifting effect, which existed in most of the piezoelectric materials [4]. In 2001, an H-type gyroscope made of LiNbO_3 with an oppositely polarized single crystal plate had been reported [5]. Due to the electromechanical coupling factor of LiNbO_3 is larger than that of LiTaO_3 for the flexural vibratory mode, this type of gyroscope is more suitable for

miniaturization, due to the fact that they can produce the same amount of vibration amplitude in a more compact size, and achieving the same level of resolution.

1.3.1 Complicated Couplings of Piezoelectric Gyroscopes

The piezoelectric gyroscope generates a null output which is called a leakage coupling effect even while the angular velocity is zero. There are usually some kinds of leakage couplings in the sensing output, and these couplings have significant influences on the performance of the piezoelectric gyroscope. Figure 1.1 illustrates the classification of unnecessary couplings. Every k is respectively expressed as below :

k_1 : electrostatic coupling between input and output.

k_2 : electromechanical coupling of driving electrode to detecting vibration mode.

k_3 : electromechanical coupling of detecting electrode to driving vibration mode.

k_4 : mechanical coupling between driving and detecting modes.

k_2 and k_3 indicate the electromechanical coupling factor, which means the ratio of transform between mechanical energy and electrical energy. They are defined as the square root of mechanical and electrical energy, and the equation is

$$k = (U_m / U_e)^{1/2} = (U_e / U_m)^{1/2} \quad (3.1)$$

U_m and U_e express the mechanical energy and electrical energy respectively. In general, the electro-mechanical coupling factor of the piezoelectric material changes

with the different resonant frequencies ω and the different piezoelectric materials. The dynamic electro-mechanical coupling factor k in resonant (short circuit) and anti-resonant (open circuit) frequency is defined by

$$k_{dn}^2 = \frac{f_a^2 - f_r^2}{f_a^2} \quad (3.2)$$

f_a^2 and f_r^2 express the anti-resonant and resonant frequency respectively.

Piezoelectric gyroscopes are usually dealt with the equivalent circuit method [10, 11]. The equivalent circuit model is constructed including electrostatic, electromechanical and mechanical leakage couplings for a piezoelectric gyroscope. However, few piezoelectric gyroscopes could be constructed the precise model due to the complexities of leakage couplings, so that the results of conventional gyroscopes can't commonly conform the expected target ; But the H-type gyroscopes have good suppression of leakage couplings from piezoelectric material [1, 2, 3]. The upper driving electrode and lower detecting electrode are divided with different sides. As a result, the divided electrodes could suppress the unnecessary k_1 , and the symmetrical H-type construction could reduce the effect of unnecessary k_4 . Therefore, the H-type shape is designed to improve the performance of the gyroscope in my study.

1.3.2 Suppression of Unnecessary Couplings

Figure 1.2 shows the configuration of the conventional fork type gyroscope [18]. The conventional fork type gyroscope is composed of different driving and detecting electrodes on the left and right arms respectively. The fork type gyroscope has two vibrating modes which are the driving mode and the detecting mode. The two modes vibrate in two direction perpendicular to each other in the plane. The driving

electrode and detecting electrode have spuriously influence on each other. Table 1 shows the electromechanical coupling coefficients of the fork gyroscope for driving and detecting electrodes.

H. Tanaka and N. Wakatsuki consider the cause of the unnecessary electrostatic coupling originated from the asymmetry of electrodes on the right and left arms [2]. Therefore, for the suppression of the unnecessary couplings, the fork type of symmetrical or similar electrodes are on both left and right arms.

Figure 1.3 shows the configuration of the H-type gyroscope. The H-type gyroscope has two resonance modes in this design, the fork mode in the detecting arms and the H mode in both the driving and detecting arms. However, in practice, there always exists some unexpected fork-mode coupling in between upper arms and lower arms, which makes it difficult to keep the fork mode motion in the upper arm only. Table.2 shows the electromechanical coupling coefficients of the H-type gyroscope including the unnecessary electromechanical coupling coefficient k of the detecting electrode and the unnecessary k of the driving electrode.

From Table 1, the unnecessary $(k_2)^2$ is 87 ppm and the unnecessary $(k_3)^2$ is 10.7 ppm in the fork type gyroscope ; From Table 2, the unnecessary $(k_2)^2$ is 9.6 ppm and the unnecessary $(k_3)^2$ is 21.5 ppm. Here, the unbalanced electrodes are defined as the asymmetrical electrode due to fabrication errors. The H-type gyroscope has a slightly unnecessary k_2 of the driving electrode to the detecting vibration mode. As a result, we know that the symmetrical electrodes on the right and left arms can suppress the unnecessary couplings.

However, as long as the displacement of the unnecessary spurious fork mode, due to electromechanical coupling, is extremely less than that compared with the maximum displacement of the driving arm, the detecting electrodes can still be designed on the surface of the lower arm without losing much of the sensing accuracy. On the other hand, the mechanical coupling, due to fabrication imperfections, of the driving mode to the detecting mode can not be negligible. Therefore, the reason for the unnecessary k of the detecting electrode to the driving mode is mainly due to the mechanical coupling. In fact, the gyroscope designs often have unbalanced electrodes due to fabrication errors. Therefore, k for the unbalanced electrodes is also simulated in this report. From Table.2, we can get an idea that the unbalanced detecting electrodes have a spurious electromechanical coupling in the detecting arms.

1.4 Survey of Adaptive Control Methods for the gyroscope

In 1998, P.W.Loveday and C.A.Rogers [22] proposed a method for the operation of vibratory gyroscopes based on the feedback control. This method can be used to determine the feasibility of replacing the traditional “mechanical balancing” operations with the feedback control algorithm, which calculates the modification to the dynamic characteristics of a piezoelectric resonator. But it is not applied to estimate the angular velocity in this approach.

Park [14] proposed adaptive control strategies for MEMS Gyroscopes in 2000. The basic idea of the adaptive control approach is to estimate the angular rate and coupling terms, due to fabrication defects, by a parameter identification algorithm. Like in other adaptive control problems, the persistent excitation condition is an important factor to estimate the unknown parameters correctly. To solve this problem, a trajectory following approach is used. By following the reference model,

the persistent excitation condition is met and estimation of all unknown parameters does converge to the correct values. The reference model in this case consists of a 2-dimensional oscillator with different resonant frequencies in each axis. As a result, the persistent excitation condition is met and the system parameters, along with the angular velocity, can be identified correctly.

Since 1990, many microelectromechanical (MEMS) gyroscopes have been developed. Adaptive control methods for MEMS gyroscopes were firstly studied in 1999 [23]. Later, in 2003, Robert P. L applied adaptive oscillator control for the drive axis of the MEMS gyroscope [24, 25].

And then, in this thesis, an adaptive control method for the piezoelectric gyroscope will be firstly proposed, and its feasibility will also be discussed.

1.5 Outline of the Thesis



In this project, we proposed a gyroscope design with the configuration similar to what have been described in section 1.3, with intention to reduce the electromechanical coupling effects. Moreover, by combining the method of adaptive control strategies described in section 1.4, all system parameters, along with the angular rate can be identified and coupling terms, due to fabrication defect, can be compensated.

The content of this report is organized as follows. Chapter 2 introduces the material properties of piezoelectric materials including its piezoelectric constitutive equations. Chapter 3 describes the dynamic equations of the designed piezoelectric gyroscope with the input/output of the system are driving voltage and piezoelectric

sensing voltage, respectively. Chapter 4 describes how we apply the adaptive algorithm to our H-type gyroscope design and shows the simulation results. Chapter 5 lists the conclusions in this study and the future works.



Chapter 2

Theory of Piezoelectric Material

2.1 Piezoelectric Material

In 1824, Brewster found that tourmaline would generate electrical charge when heated, what is called “pyroelectricity”.

In 1880, the brothers Pierre Curie and Jacques Curie predicted and demonstrated piezoelectricity of certain material. They showed that crystals of tourmaline, quartz, and Rochelle salt (sodium potassium tartrate tetrahydrate) generated electrical polarization from mechanical stress.

Piezoelectricity is an interaction between electrical and mechanical systems. Piezoelectric materials have two main effects. One is direct piezoelectric effect, and the other is converse piezoelectric effect. The direct piezoelectric effect is a fact that piezoelectric materials produce electric polarization by forcing mechanical stress. On the contrary, the conversely piezoelectric effect is a fact that piezoelectric materials produce deformation by applying electric field.

The electromechanical coupling effect of piezoelectric materials is used widely in engineering. By means of above two effects, many kinds of actuators and sensor could be made. But there are some disadvantages to worthy of concern in application of piezoelectric materials; for example, it usually produces unnecessary coupling effects in any direction perpendicular to driving axis in the process of applying voltage.

In order to improve the accuracy and stability of gyroscopes, the null signal suppression of leakage couplings is significant. These null couplings have two main sources: mechanical and electromechanical couplings. The former produces from the manufacture defects, and the latter is due to piezoelectric property between the driving and detecting electrode. These troublesome cases of leakage couplings could be improved by means of changing the designed structure either or dealing with control stratagems, and then the resolution of gyroscopes would be improved in the expected situation.

In general, piezoelectric materials have advantages of high strength, high bandwidth, and, short response time, are used widely in vibratory gyroscopes.

2.2 Piezoelectric Constitutive Equations

Piezoelectric Constitutive Equation is described mathematically as below :

d-form :

$$\begin{cases} \mathbf{S} = \mathbf{s}_E * \mathbf{T} + \mathbf{d}^t * \mathbf{E} \\ \mathbf{D} = \mathbf{d} * \mathbf{T} + \boldsymbol{\varepsilon}_T * \mathbf{E} \end{cases} \quad (2.1)$$

The four state variables (**S**, **T**, **D**, and **E**) can be rearranged arbitrarily to give an additional 3 forms for a piezoelectric constitutive equation by mathematics operation. It is possible to transform piezoelectric constitutive data in one form to another form. In addition to the coupling matrix **d**, they contain the other coupling matrices **e**, **g**, or **h** in another 3 forms. What follows another 3 piezoelectric constitutive equations and their mutual transformations :

e-form :

$$\begin{cases} T = c_E * S + e^t * E \\ D = e * S + \epsilon_S * E \end{cases} \quad (2.2)$$

g-form :

$$\begin{cases} S = s_D * T + g^t * D \\ E = -g * T + \epsilon_T^{-1} * D \end{cases} \quad (2.3)$$

h-form :

$$\begin{cases} T = c_D * S + h^t * D \\ E = -h * S + \epsilon_S^{-1} * D \end{cases} \quad (2.4)$$

Generally speaking, common publish material data exhibit **d** and **g**, whereas certain software such as finite element codes requires piezoelectric data entered as **e**. So it is essential to be the other forms for our convenience. All the descriptions of matrix variables used in the piezoelectric constitutive equations are shown in Table 3 and Table 4.

The four forms described above could be combined with the matrix form as follows. Thereinafter, for example, there are the d-form LiNbO₃ constitutive equations for a full matrix form. All values of the parameters in matrix could be found in Table 5 – Table 9.

$$\begin{bmatrix} S_1 \\ S_2 \\ S_3 \\ S_4 \\ S_5 \\ S_6 \\ D_1 \\ D_2 \\ D_3 \end{bmatrix} = \begin{bmatrix} s_{11} & s_{12} & s_{13} & s_{14} & 0 & 0 & 0 & -2d_{y2} & d_{z1} \\ s_{12} & s_{11} & s_{13} & -s_{14} & 0 & 0 & 0 & d_{y2} & d_{z1} \\ s_{13} & s_{13} & s_{33} & 0 & 0 & 0 & 0 & 0 & d_{z3} \\ s_{14} & -s_{14} & 0 & s_{44} & 0 & 0 & 0 & d_{x5} & 0 \\ 0 & 0 & 0 & 0 & s_{44} & 2s_{14} & d_{x5} & 0 & 0 \\ 0 & 0 & 0 & 0 & 2s_{14} & 2(s_{11} - s_{12}) & -2d_{y2} & 0 & 0 \\ 0 & 0 & 0 & 0 & d_{x5} & -2d_{y2} & \epsilon_{xx} & 0 & 0 \\ -2d_{y2} & d_{y2} & 0 & d_{x5} & 0 & 0 & 0 & \epsilon_{xx} & 0 \\ d_{z1} & d_{z1} & d_{z3} & 0 & 0 & 0 & 0 & 0 & \epsilon_{zz} \end{bmatrix} \quad (2.5)$$

The meaning of the suffixes of the symbols for S and D are respectively expressed as below ; all meanings of the suffixes of all the symbols is shown in Figure :

S_1 : x strain ;

S_2 : y strain ;

S_3 : z strain ;

S_4 : yz shear strain ;

S_5 : xz shear strain ;

S_6 : xy shear strain ;

D_1 : x electric charge density ;

D_2 : y electric charge density ;

D_3 : z electric charge density ;



The other three forms (e, g, and h-form) could be done similarly, and the relationships of transformation for four forms are :

$$\text{e-form : } c_E = \frac{1}{s_E} \text{ , } \varepsilon_s = \varepsilon_T (1 - k_d^2) \text{ , } e = \frac{d}{s_E} \quad (2.6)$$

$$\text{g-form : } s_D = s_E (1 - k_d^2) \text{ , } g = \frac{d}{\varepsilon_T} \quad (2.7)$$

$$\text{h-form : } c_D = \frac{1}{s_E (1 - k_d^2)} \text{ , } h = \frac{k_d^2}{d (1 - k_d^2)} \quad (2.8)$$

The different relationships of transformation are applied for different actuators or sensors for convenience.



Chapter 3

Preliminary Design of Piezoelectric Gyroscope

The conceptual design of H-type piezoelectric gyroscope is presented in this chapter. As requested by the adaptive control algorithm, we designed a long upper arm and a short lower arm for our H-type vibratory gyroscopes. The insulation layers, which were utilized to minimize the electrostatic coupling, is also presented and discussed. Lastly, an approximated 2nd order model for our H-type gyroscope is obtained, based on the FEM simulation results, for the subsequent adaptive control strategy.

3.1 Design of Piezoelectric Gyroscope Configuration

As requested by the subsequent adaptive control strategy, the designed piezoelectric gyroscopes must be actuated and sensed in both fork-mode and H-mode simultaneously. The requirement defeats the existing H-type gyroscope designs proposed in [2, 3], which the Y (fork) mode existed only in actuation arms and the H mode in both the driving and detecting arms. Here we proposed two conceptual designs to meet this performance requirement. The case I design is a Y-type gyroscope and the case II is a H-type gyroscope with different arm lengths. Both designs based on the bimorph bending motion of piezoelectric materials to achieve its resonance. The basic equations that described the bimorph motion is listed in APPENDIX I.

3.1.1 Case I: The Y-type piezoelectric gyroscopes

In order to reduce the electromechanical coupling effects between driving and detecting electrodes, we propose a model shown in Figure 3.4. The symmetrical

driving and detecting electrodes suppress coupling effects, and the intermediate isolation layer among driving and detecting electrodes prevents the voltage feedthrough from driving voltage electrode to sensing voltage electrodes. Most importantly, this structure can be actuated and their respectively vibrating motion can be measured in both Y-mode and H-mode. However, it is a debatable point whether the vibratory arm which driving and detecting electrodes are put together is still the pure bending motion. Moreover, the leakage electric coupling between the driving and detecting electrodes could also be the problem, even though the insulation layers are inserted.

3.1.2 Case II: The H-type piezoelectric gyroscopes

To benefit the advantages from the existing H-types gyroscopes such as less electrostatic coupling [2, 3], we designed a newly H-type gyroscope with the Y mode is advisedly arisen in both the driving and detecting arms so that the gyroscope have an ability to control and measure the motion in dual axes. This is done by deliberately using a thin connecting bar in between left and right arms and different arm lengths of upper arms and lower arms. After done so, the effect of the quadratic spring is worsen and is expected to be dealt with by the subsequent adaptive control strategies.

The amplitude of the vibratory mode changes with the size of a gyroscope, and the resonant frequencies of the two modes also depend on arm thickness, arm width and arm length. Figure 3.5 shows the size of the designed gyroscope, which is advisedly established the different size between driving and detecting arms. The deflection of upper arms will arise in our design configuration while applying force to the lower arms in the Z-direction in Figure 3.6, and that is the Y-mode vibratory of the newly

designed gyroscope. Two vibratory modes simulated by FEM are shown in Figure 3.7 and Figure 3.8, and lateral views are shown in Figure 3.9 and Figure 3.10. Their resonant frequencies are respectively 214 kHz for Y mode and 220 kHz for H mode.

Based on the design with enough space divided the driving electrode from the detecting electrode, and which has the ability to control and measure the motion in dual axes. The case II proposes a more suitable model than the case I for the designed gyroscope to work with the adaptive control strategies.

3.2 Electrostatic Coupling Analysis and Reduction

With the permittivity property of piezoelectric materials, the output signal of the piezoelectric gyroscope contains unnecessary electrostatic leakage coupling from the driving electrode to the detection electrode as shown in Figure 3.11. That is the k_1 term described in section 1.3.1. Because the leakage output passes through the intermediate layer of the H-gyro between driving and sensing electrode, it's possible to set up an isolation layer to prevent the unnecessary leakage signal. Figure 3.12 shows the concept design with the intermediate layer GND. If the method works, the frequency response of the gyroscope will have a similar response and the leakage would be minimized.

Figure 3.13 and Figure 3.14 shows the FEM simulation results of cases with and without isolation layers. Figure 3.13 shows the frequency response of the designed gyroscope with setting up the isolating material in the intermediate layer, and there is no any leakage voltage passing through the intermediate layer of the H-gyro. Figure 3.14 shows the frequency response of the designed gyroscope without any restriction in the intermediate layer. Moreover, Figure 3.15 shows the frequency response of

the gyroscope pasting with the intermediate planar electrode GND. As the above Figures indicate, the frequency response of Figure 3.15 is almost the same with that of Figure 3.13, and different from that of Figure 3.14. That is to say, our design with the intermediate layer GND can effectively suppress the leakage electrostatic coupling effect of H-gyro.

3.3 Dynamics for the Designed Gyroscope

This section describes the dynamic motion and how we obtain an approximated 2nd order dynamic equation of the designed H-gyro. Then, we will model the mechanical coupling term of spring constant and use these parameters to be simulated in next chapter.

3.3.1 Dynamic Motion of the Designed Gyroscope

The relative deflection percentage between upper and lower arms in the vibratory mode is presented in this section. According to the configuration of the designed model in Figure 3.5, Figures 3.16 shows the relative displacements U_{zn}/U_{zo} at node $n = \#1\sim17$ for Y vibratory mode. U_{zn} is the displacement of every divided averagely node in the y direction, and U_{zo} is the maximum displacement at the short one of two arms. According to the result of Figure 3.16, we can confirm the amplification factor of detecting output voltage in the detecting arms because of the asymmetrical motion between upper and lower arms.

Besides, Figures 3.17 shows the relative displacements U_{yn}/U_{yo} at node $n = \#1\sim17$ for H vibratory mode, U_{yn} is the displacement of every divided averagely node in the y direction, and U_{yo} is the maximum displacement at the short arm ends. According

to the result of Figure 3.16, the H vibrating mode also amplifies the displacement in the long arm.

According to the Figure 3.16 and Figure 3.17, we can know the deflection in the upper arms is amplified in the dynamic motion of the designed gyroscope, that is to say, we can detect larger output signal in the detecting arms than the existing H-gyro due to the design of long detecting arms. It will be helpful to measure the output signals of detecting arms.

3.3.2 Frequency Response & Approximate 2nd Order Model

With the resonant frequencies of the two axes as mentioned above, the frequency characteristics of the transfer function from the driving arm (short arm) to the detecting electrode (long arm) can be analyzed in the harmonic analysis simulated by FEM. In this section, the V_{in}/V_{out} voltage relationship between the driving and detecting electrode is obtained instead of the relationship between the force and displacement. The main reason is that the frequency characteristics of the V_{in}/V_{out} can directly show the relationship between driving electrode and detecting electrode without transferring the displacement signal and force signal to voltage signal. On the other hand, it is more convenient to deal with our data. Detailed account for the transferred relationship is given below.

Equation (3.1) shows the basic dynamic equations of the conventional two-axes vibratory gyroscope, $2M\Omega\dot{y}$ and $2M\Omega\dot{x}$, are due to the Coriolis acceleration and the two terms are usually used to measure the angular velocity Ω .

$$\begin{cases} M\ddot{x} + d_{xx}\dot{x} + d_{xy}\dot{y} + k_{xx}x + k_{xy}y = \tau_x + 2M\Omega\dot{y} \\ M\ddot{y} + d_{xy}\dot{x} + d_{yy}\dot{y} + k_{xy}x + k_{yy}y = \tau_y - 2M\Omega\dot{x} \end{cases} \quad (3.1)$$

M is a mass, d and k are damping and spring term respectively. To match up the adaptive control strategies, we first divide the equation (3.1) by the mass M and get :

$$\begin{aligned}\ddot{x} + \frac{d_{xx}}{M} \dot{x} + \frac{k_{xx}}{M} x &= \frac{\tau_x}{M} + 2\Omega \dot{y} \\ \ddot{y} + \frac{d_{yy}}{M} \dot{y} + \frac{k_{yy}}{M} y &= \frac{\tau_y}{M} - 2\Omega \dot{x}\end{aligned}\quad (3.2)$$

And with properties of piezoelectric materials, there is constant relationship (K_v , K_m) either between the deflection and sensing voltage in the detecting arms, or between the control input voltage and control input force.

$$x = K_v \cdot V ; \tau = K_m \cdot V_{in} \quad (3.3)$$

Then, we can obtain dynamic equations with V_{in}/V_{out} voltage relationship :

$$\begin{aligned}\ddot{V}_x + \frac{d_{xx}}{M} \dot{V}_x + \frac{k_{xx}}{M} V_x &= \frac{K_m \cdot V_{in-x}}{K_v M} + 2\Omega \dot{V}_y \\ \ddot{V}_y + \frac{d_{yy}}{M} \dot{V}_y + \frac{k_{yy}}{M} V_y &= \frac{K_m \cdot V_{in-y}}{K_v M} - 2\Omega \dot{V}_x\end{aligned}\quad (3.4)$$

Now, equation (3.4) is model with V_{in}/V_{out} relationship which is suited for the compensation of adaptive control strategies. Frequency responses of Y and H modes are respectively simulated by FEM.

The adaptive strategies in section 4.1 are suitable for a 2nd order model. But the identity of the H-type model is a high order system. Here, we get an approximated 2nd order model by utilizing curve fitting method around the appropriate operation frequency. Figure 3.18 and Figure 3.19 show the conception of curve fitting method and red curve is a standard 2nd order system. Blue curve is real frequency response and red curve is an approximate 2nd order model by curve fitting. As the result of using the adaptive algorithm for the approximated 2nd order model, all the parameters and angular velocity are expected to converge to the correct values.

The approximated 2nd order model can be described as follows.

$$\begin{aligned}\ddot{V}_x + D_{xx}\dot{V}_x + K_{xx}V_x &= V_x + 2\Omega\dot{V}_y \\ \ddot{V}_y + D_{yy}\dot{V}_y + K_{yy}V_y &= V_y - 2\Omega\dot{V}_x\end{aligned}\quad (3.5)$$

where

$$D_{xx} = \frac{d_{xx}}{M}; K_{xx} = \frac{k_{xx}}{M}; V_x = \frac{K_m \cdot V_{in-x}}{K_v M} \quad (3.6)$$

That is proven by the same way for the parameters of y axis and all the parameters are shown in Table 12.

3.3.3 Modeling the Electromechanical Coupling

Dynamic coupling effects are necessarily eliminated in a high-resolution gyroscope. In practice, small fabrication imperfections usually occur and arise due to the asymmetric spring and damping terms, which results in dynamic coupling between two axes even under zero angular velocity. So these fabrication coupling effects are major factors limiting the performance of gyroscopes. Aside from fabrication imperfections, the essential electromechanical couplings of piezoelectric material are also factors limiting the performance.

Now, we try to model the unnecessary coupling terms [14]. Assume that the real spring constants are k_1 and k_2 , and the real spring axes are titled by angel α from the driving and detecting axis for ideal gyroscope because of unnecessary couplings.

Let $[x, y]$ be the ideal axes and $[x', y']$ be the real coordinates. So the real axes and ideal axes are related by

$$\begin{bmatrix} x' \\ y' \end{bmatrix} = \begin{bmatrix} \cos \alpha & \sin \alpha \\ -\sin \alpha & \cos \alpha \end{bmatrix} \begin{bmatrix} x \\ y \end{bmatrix} \quad (3.7)$$

Then, the relationship between forces and displacement in the real axes is given by

$$\begin{bmatrix} F'_x \\ F'_y \end{bmatrix} = \begin{bmatrix} k_1 & 0 \\ 0 & k_2 \end{bmatrix} \begin{bmatrix} x' \\ y' \end{bmatrix} \quad (3.8)$$

the relationship between forces and displacement in the ideal axes is therefore given by

$$\begin{bmatrix} F_x \\ F_y \end{bmatrix} = \begin{bmatrix} k_x & k_{xy} \\ k_{xy} & k_y \end{bmatrix} \begin{bmatrix} x \\ y \end{bmatrix} \quad (3.9)$$

And,

$$\begin{bmatrix} F'_x \\ F'_y \end{bmatrix} = \begin{bmatrix} \cos \alpha & \sin \alpha \\ -\sin \alpha & \cos \alpha \end{bmatrix} \begin{bmatrix} F_x \\ F_y \end{bmatrix} \quad (3.10)$$

Therefore, we get

$$\begin{bmatrix} F'_x \\ F'_y \end{bmatrix} = \begin{bmatrix} k_1 & 0 \\ 0 & k_2 \end{bmatrix} \begin{bmatrix} \cos \alpha & \sin \alpha \\ -\sin \alpha & \cos \alpha \end{bmatrix} \begin{bmatrix} x \\ y \end{bmatrix} \quad (3.11)$$

$$\begin{bmatrix} F'_x \\ F'_y \end{bmatrix} = \begin{bmatrix} \cos \alpha & \sin \alpha \\ -\sin \alpha & \cos \alpha \end{bmatrix} \begin{bmatrix} k_x & k_{xy} \\ k_{xy} & k_y \end{bmatrix} \begin{bmatrix} x \\ y \end{bmatrix} \quad (3.12)$$

Compare with the above two equations, we get

$$k_x = k_1 \cos^2 \alpha + k_2 \sin^2 \alpha = \frac{k_1 + k_2}{2} + \frac{k_1 - k_2}{2} \cos 2\alpha \quad (3.13)$$

$$k_y = k_1 \sin^2 \alpha + k_2 \cos^2 \alpha = \frac{k_1 + k_2}{2} + \frac{k_2 - k_1}{2} \cos 2\alpha \quad (3.14)$$

$$k_{xy} = (k_1 - k_2) \sin \alpha \cos \alpha = \frac{k_1 - k_2}{2} \sin 2\alpha \quad (3.15)$$

Therefore, we can calculate the electromechanical coupling term K_{xy} by above equations. And we will assume damping parameter D_{xy} due to the fabrication imperfection in my simulation. All the estimations of the unknown parameters are shown in Table 12.

3.3.4 Convergence Analysis of Result by ANSYS

Different mesh size controls of the ANSYS program adequate for the different model we are analyzing. In this case, we are going to specify the mesh size of the designed gyroscope. Figure 3.20 and Figure 3.21 show the simulative results in the different mesh density. As a result, we can find the suitable mesh size for our model. Therefore, we can verify the validity of the result by the convergent analysis. As shown in Figure 3.20 and Figure 3.21, the reasonable mesh density is for our designed gyroscope is obtained.

Chapter 4

Adaptive Control of Piezoelectric Gyroscope

To verify the feasibility of the adaptive control strategies, the designed model presented in previous chapter will be employed to simulate in this chapter. After the configuration of the gyroscope is accomplished, we begin to deal with the coupling terms such as k_2 and k_3 described in section 1.3. They are able to be eliminated with H-type configuration by FEM. And the mechanical-thermal and electrical-thermal noises are also considered. We use the adaptive control method to identify the unknown coupling terms and we can obtain an accurate angular velocity at the same time.

4.1 Adaptive Control Strategies

Park [14] proposed adaptive control strategies for MEMS Gyroscopes. The basic idea of the adaptive control approach is to treat the angular rate, along with the unknown coupling terms due to fabrication defects, as the parameters which will be identified by using adaptation algorithms. First, the adaptive control problems of the gyroscope is described as follows : Given the gyroscope plant equation with unknown constant parameters D , K and Ω .

$$\ddot{q} + D\dot{q} + Kq = \tau - 2\Omega\dot{q} \quad (4.1)$$

where

$$q = \begin{bmatrix} x \\ y \end{bmatrix} \quad (4.2)$$

D , K and Ω are respectively described as follows :

$$D = \begin{bmatrix} D_{xx} & D_{xy} \\ D_{xy} & D_{yy} \end{bmatrix} \quad (4.3)$$

$$K = \begin{bmatrix} K_{xx} & K_{xy} \\ K_{xy} & K_{yy} \end{bmatrix} \quad (4.4)$$

$$\Omega = \begin{bmatrix} 0 & -\Omega_z \\ \Omega_z & 0 \end{bmatrix} \quad (4.5)$$

where

$$K = K^T > 0, \quad D = D^T \geq 0, \quad \text{and} \quad \Omega = -\Omega^T \quad (4.6)$$

In the adaptive control strategies by Park, the persistent excitation condition is an important factor to estimate the unknown parameters correctly. To match this condition, a trajectory following approach is used. By following the reference model, the persistent excitation condition is met and all unknown parameters converge. The reference model is generated by an ideal oscillator and the trajectory of the gyroscope is controlled to follow that of the reference model. The reference model is defined as

$$\ddot{q}_m + K_m q = 0 \quad (4.7)$$

where

$$q_m = \begin{bmatrix} x_m \\ y_m \end{bmatrix} \quad (4.8)$$

$$K_m = \begin{bmatrix} \omega_1^2 & 0 \\ 0 & \omega_2^2 \end{bmatrix}, \quad \omega_1 \neq \omega_2 \quad (4.9)$$

Here, what has to be noticed is that resonant frequencies of two axes of the reference model must be unmatched by persistent excitation condition [14]. τ is the control law based on measuring q and \dot{q} , and the control law is chosen to be

$$\tau = \hat{D}\dot{q}_m + \hat{R}q_m + 2\hat{\Omega}\dot{q}_m + \tau_0 \quad (4.10)$$

Where $R = K - K_m$, \hat{D} , \hat{R} , $\hat{\Omega}$ are respectively estimates of D , K and Ω ,

and

$$\tau_0 = -\gamma \dot{e}_p \quad (4.11)$$

where

$$\gamma = \begin{bmatrix} \gamma_1 & 0 \\ 0 & \gamma_2 \end{bmatrix} \quad (4.12)$$

$$e_p = q - q_m \quad (4.13)$$

Now, the trajectory error dynamics becomes

$$\ddot{e}_p + (\gamma + D + 2\Omega)\dot{e}_p + Ke_p = \tilde{D}\dot{q}_m + \tilde{R}q_m + 2\tilde{\Omega}\dot{q}_m \quad (4.14)$$

Then define the Lyapunov function

$$V = \frac{1}{2}(\dot{e}_p^T \gamma \dot{e}_p + e_p^T \gamma K e_p + \text{trace}(\gamma_D^{-1} \tilde{D} \tilde{D}^T + \gamma_R^{-1} \tilde{R} \tilde{R}^T + \gamma_\Omega^{-1} \tilde{\Omega} \tilde{\Omega}^T)) \quad (4.15)$$

The derivative of the Lyapunov function is

$$\begin{aligned} \dot{V} = & -\dot{e}_p^T \gamma (\gamma + D + 2\Omega) \dot{e}_p \\ & + \text{trace} \left\{ \begin{aligned} & \tilde{D} \left(\gamma_D^{-1} \dot{\tilde{D}}^T - \frac{1}{2} \dot{q}_m \tau_0^T - \frac{1}{2} \tau_0 \dot{q}_m^T \right) + \tilde{R} \left(\gamma_R^{-1} \dot{\tilde{R}}^T - \frac{1}{2} q_m \tau_0^T - \frac{1}{2} \tau_0 q_m^T \right) \\ & + \tilde{\Omega} \left(\gamma_\Omega^{-1} \dot{\tilde{\Omega}}^T - \dot{q}_m \tau_0^T - \tau_0 \dot{q}_m^T \right) \end{aligned} \right\} \quad (4.16) \end{aligned}$$

Here, the key we need to pay attention is that “ $(\gamma + D + 2\Omega)$ ” must be positive definite such that $V \cdot \dot{V} < 0$ and Lyapunov function converges.

Therefore, the parameter adaptive laws are as follows.

$$\dot{\hat{D}} = \frac{1}{2} \gamma_D (\tau_0 \dot{q}_m^T + \dot{q}_m \tau_0^T) \quad (4.17)$$

$$\dot{\hat{R}} = \frac{1}{2} \gamma_R (\tau_0 q_m^T + q_m \tau_0^T) \quad (4.18)$$

$$\dot{\hat{\Omega}} = \gamma_\Omega (\tau_0 \dot{q}_m^T - \dot{q}_m \tau_0^T) \quad (4.19)$$

The above parameter adaptive laws lead to $\dot{V} \leq -\dot{e}_p^T \gamma^2 \dot{e}_p \leq 0$, which ensure that all the parameter estimates of the gyroscope converge to their true values.

4.2 Estimation of Noise

For gyroscopes designed for small-size applications, it is expectable that noise floor has a large influence on the resolution, so the question about the fundamental noise limit of the gyroscope is vital. In general, the two noise sources of piezoelectric transducer, the mechanical-thermal noise of the damped mechanical harmonic oscillator and the electrical-thermal noise of the piezoelectric material are often the limiting noise components for gyroscope. This subsection discusses the estimated noise of the designed gyroscope, and simulation results with adaptive control strategies are presented in next section.

4.2.1 Mechanical-thermal Noise

A brownian system resulting in the mechanical-thermal noise is an example of noise-related theory that is applied to various natural phenomena. Several studies have emphasized the features of this phenomenon and its complexity arising from sensitivity to structural parameters [26, 27]. PSD (power spectral density) is a general unit describing how the power (or variance) of a time series is distributed with frequency. Mathematically, a standard PSD of noise is white noise (it is independent

of ω and its plot against frequency is "flat") which has the same power at every frequency.

$$S_m(f) = \sqrt{4K_B TR} \left(N / \sqrt{\text{Hz}} \right), f \geq 0 \quad (4.20)$$

K_B is Boltzmann's constant ($1.38 \times 10^{-23} \text{ J/K}$) and T is the absolute temperature.

The PSD (power spectral density) of the fluctuating force related to any mechanical resistance.

In our designed H-gyro, some parameters are shown as follows and S_m of mechanical-thermal noise can be obtained.

$$f = 220 \text{ kHz}, Q = 100, R = 4.13 \times 10^{-4} \text{ N} \cdot \text{s/m}, T = 300^\circ \text{ K}$$

$$\text{Then, we obtain } S_m = 2.62 \times 10^{-12} \text{ N}/\sqrt{\text{Hz}}.$$

4.2.2 Electrical-thermal Noise

The mechanism of the electrical-thermal noise is related with losses in the piezoelectric material and depends on its loss factor or dissipation factor, which is inverse of the PE material's quality factor [28].

By definition[x], loss factor η equals

$$\eta = \frac{1}{\omega CR} \quad (4.21)$$

The Power spectral density of the electrical-thermal noise is given

$$S_e = \sqrt{4K_B TR_n} \left(V / \sqrt{\text{Hz}} \right) \quad (4.22)$$

These equations can be used for the calculation of the fundamental noise limit of piezoelectric materials as their parameters are known or can be obtained.

K_B is Boltzmann's constant ($1.38 \times 10^{-23} \text{ J/K}$) and T is the absolute temperature. Here, R_n is an equivalent noise resistor which is related with frequency ($\omega = 2\pi f$), capacitor (C), and loss factor (η).

$$R_n = \frac{1}{\omega C \left(\eta + \frac{1}{\eta} \right)} \quad (4.23)$$

In our designed H-gyro, some parameters are shown as follows and S_e of electrical-thermal noise can be obtained.

$$f = 220 \text{ kHz}, \eta = 0.01, C = 26.7 \text{ pF}, T = 300^\circ \text{ K}$$

$$\text{Then, we obtain } S_e = 2.12 \times 10^{-8} \text{ V}/\sqrt{\text{Hz}}.$$

4.3 Simulation Results and Discussion

Some simulations are implemented by MATLAB software package. These simulation results are shown to verify the feasibility of the designed gyroscope associated with the adaptive control strategies.

In this case, comparing the mechanical-thermal noise with the electrical-thermal noise, the electrical-thermal noise has a more critical influence on the output signal of the detecting electrode than that of mechanical-thermal noise. Their PSD, position noises and velocity noises are shown in Table 10.

A simulation using the preliminary design parameters was conducted, and the noise of the gyroscope was included, too. All gyroscope parameters in the model are summarized in Table 11 and Table 12. The simulation results are also presented in this section. To verify the performance of the gyroscope, we calculate the standard deviation of the angular velocity and compare with the performance of the open-loop

mode.

Before starting the simulation, an important issue has to be noted is how we specify the reference model. In adaptive control strategies, the gyroscope is designed to follow the reference model such that the parameters of the gyroscope are convergent. On the other hand, the reference trajectory is generated by an ideal oscillator and the trajectory of the real gyroscope is controlled to follow that of the reference model. Therefore, the setting value of the amplitude of vibration of the reference trajectory must meet certain physical behaviors of the real gyroscope. The reference gyroscope must be met with the gyroscope in real world while we set up the dynamic characteristics of the reference model in our simulation.

Such an Adaptive mode of operation, using reference model signals instead of the real measurement signals, has the advantages that the reference signals q_m , \dot{q}_m are not contaminated by measurement noises. Therefore, the performance of the gyroscope is determined by measurement signals of control input τ . How we reduce the noises of the measurement signals in the sensing electrode is the key factor for improving the resolution of the gyroscope.

Some simulation results are shown. Figure 4.1 and Figure 4.2 respectively show the trajectories of the proof mass and the tracking errors of x and y axes. The various estimation errors of D, R in the gyroscope are shown in Figure 4.3 and Figure 4.4 respectively. The estimate of angular velocity Ω response to a constant input angular velocity is shown in Figure 4.5, and in this figure, the standard deviation of the angular velocity estimate error is obtained.

In our simulation, the adaptive control gains are as shown in Table 13. Figure 4.3, Figure 4.4 and Figure 4.5 show that the parameters D, Ω of the gyroscope

are identified correctly, but the parameter R could not meet the specific value ideally. From equation (4.18), the convergence of R term is determined by dual-axes error signals and some control gains. Here, we notice the Figure 4.2 reveals the converging time of the error signal is about 1 ms time, and more noteworthy is the large difference scale between D and R . From the reasons mentioned above, it seems reasonable to conclude the converging rate of error signal is fast enough for the D terms, but not enough for the R in the simulation with the selected control gains. Fortunately, even if the R terms does not converge ideally, this doesn't affect the validity of the angular velocity Ω . As mentioned above, the adjustment of the adaptive control gains is also an important issue for fine convergence of parameters. In this thesis, the optimization of the adaptive control gains will not be discussed.

The resolution of the open-loop gyroscope can be estimated in rough by calculating the noise floor, and the Brownian noise floor equivalent angular velocity is given roughly by [14]

$$\Omega \approx \sqrt{\frac{2K_B T}{MQ_y X_0^2 \omega_n}} \quad (4.24)$$

Equation (4.24) is an important design index for determining the ultimate achievable resolution of the open-loop mode operating with an ideal low-pass filter. A large resonant frequency generally is a better choice in terms of achieving high resolution for the gyroscope. Let us calculate the open-loop resolution of the designed gyroscope having the following parameters :

$$M = 3.036 \times 10^{-8} \text{ kg} ; Q_y = 100 ; X_0 = 9.6 \times 10^{-9} \text{ m} ; \omega_n = 2 \cdot \pi \cdot 215 \text{ KHz}$$

Then we obtain $\Omega \approx 0.0047 \text{ rad/s} = 0.2693 \text{ deg/s}$.

Consequently, the resolution of the gyroscope is expected to be improved with applying adaptive algorithms. In our simulation, with the appropriate adaptive control gains, the Close-loop resolution $\Omega \approx 1.104 \times 10^{-4} \text{ rad/s} = 0.0063 \text{ deg/s}$ can be achieved. As a result, the resolution of the close-loop control mode is obviously better than that of open-loop mode.

Moreover, let us now look deeper into the control input voltage of the dual axes, Figure 4.6 and Figure 4.7 respectively show the control voltage of x and y axes. As the figures indicate, the control voltages of dual-axes driving arm are below 10 V. It helps to realize the designed H-gyro concerning with practicality.



Chapter 5

CONCLUSION AND FUTRE WORKS

5.1 Conclusion

In this work, the preliminary conceptual design of the vibratory gyroscope is presented and one feasible operation associated with the adaptive control strategies is proposed. This design is based on the H-type gyroscope, which has the advantage of reducing electrostatic feedthrough and large output signals. Moreover, an effective suppression of leakage electrostatic coupling is proposed by utilizing the design with the intermediate layer GND of H-gyro. The fabrication errors and the mechanical coupling were identified by the adaptive algorithms and null out along the operation of this gyroscope. With consideration for noises arising in the designed gyroscope, a 0.0063deg/s resolution can be achieved and the control voltages of dual-axes driving arms are below 10 V in our simulations.

5.2 Future Works

In this thesis, we designed a MEMS PZT gyroscope which is expected to fabricate based on the in-situ fabrication process. However, more complete simulation and experiments must be accomplished in future. There is still room for further investigation in this study. Some future works are summarized below.

1. Mechanical Q-values and resonant frequencies of two axes have a complicated relationship with temperature characteristics. In this paper, the temperature effect due to the piezoelectric material is not considered.

2. Different piezoelectric materials have different properties, which will influence the constant values of the stiffness matrix, piezoelectric matrix and dielectric matrix. Moreover, different cut angle of the piezoelectric material would change values of the matrix. In other words, there will be an optimal piezoelectric material and cut angle for the proposed gyroscope design.
3. In order to fabricate the proposed PZT gyroscope by so-gel process, the configuration and electric wiring with planar configuration is preferred. One of the planar configurations that can meet our performance requirements is shown in Figure 5.1.



APPENDIX I

Piezoelectric materials are used in many different types of electromechanical transducers. Now we discuss the motion of the bending model. According to the Kirchhoff & Love relations between strain and deflection of piezoelectric materials [21], ignore $(1 + z/R_i)$ term, the relations become

$$S_1 = \frac{1}{A_1} \left[\frac{\partial U}{\partial \alpha_1} + \frac{V}{A_2} \frac{\partial A_1}{\partial \alpha_2} + W \frac{A_1}{R_1} \right] \quad (I.1)$$

$$S_2 = \frac{1}{A_2} \left[\frac{\partial U}{\partial \alpha_2} + \frac{V}{A_1} \frac{\partial A_2}{\partial \alpha_1} + W \frac{A_2}{R_2} \right] \quad (I.2)$$

$$S_3 = \frac{\partial W}{\partial z} \quad (I.3)$$

$$S_4 = A_2 \frac{\partial}{\partial z} \left[\frac{V}{A_2} \right] + \frac{1}{A_2} \left[\frac{\partial W}{\partial \alpha_2} \right] \quad (I.4)$$

$$S_5 = A_1 \frac{\partial}{\partial z} \left[\frac{U}{A_1} \right] + \frac{1}{A_1} \left[\frac{\partial W}{\partial \alpha_1} \right] \quad (I.5)$$

$$S_6 = \frac{A_1}{A_2} \frac{\partial}{\partial \alpha_2} \left[\frac{U}{A_1} \right] + \frac{A_2}{A_1} \frac{\partial}{\partial \alpha_1} \left[\frac{V}{A_2} \right] \quad (I.6)$$

where U 、 V 、 W are respectively total deflection of x 、 y 、 z coordinates.

$$U(\alpha_1, \alpha_2, z) = u(\alpha_1, \alpha_2) + z\beta_1(\alpha_1, \alpha_2) \quad (I.7)$$

$$U(\alpha_1, \alpha_2, z) = v(\alpha_1, \alpha_2) + z\beta_2(\alpha_1, \alpha_2) \quad (\text{I.8})$$

$$W(\alpha_1, \alpha_2, z) = w(\alpha_1, \alpha_2, z) \quad (\text{I.9})$$

$$\beta_1 = \frac{u}{R_1} - \frac{1}{A_1} \frac{\partial w}{\partial \alpha_1} \quad (\text{I.10})$$

$$\beta_2 = \frac{v}{R_2} - \frac{1}{A_2} \frac{\partial w}{\partial \alpha_2} \quad (\text{I.11})$$

u , v , w are respectively membrane displacement of x , y , z , and β_1 , β_2 are defined as shear strain or bending strain. A_1 , A_2 are defined as Lamé parameters or fundamental form parameters. The fundamental form parameters above are shown in Table 14, which are different due to the different configuration.

Now we consider the planar actuator (sensor), so-called planar actuator (sensor) is that the stresses (T_3 , T_4 and T_5) of the vertical coordinate are smaller extremely than that (T_1 , T_2 and T_6) of the horizontal. When these planar actuators are combined laminated construction, the equations are described as follow :

$$L_1(u, v, w) = A_1 A_2 (\rho h \ddot{u} + f_1) + L_1(d_{31}, d_{32}, d_{36}) \quad (\text{I.12})$$

$$L_2(u, v, w) = A_1 A_2 (\rho h \ddot{v} + f_2) + L_2(d_{31}, d_{32}, d_{36}) \quad (\text{I.13})$$

$$L_3(u, v, w) = A_1 A_2 (\rho h \ddot{w} + f_3) + L_3(d_{31}, d_{32}, d_{36}) \quad (\text{I.14})$$

where $L_i(u, v, w)$, $L_i(d_{31}, d_{32}, d_{36})$; $i=1, 2, 3$ are respectively deflection function of differential operator and piezoelectricity function of differential operator [13] ; 1 , 2 , 3 are respectively x , y , z coordinates.

For a planar double-decked actuator (sensor), the vertical deflection of the planar double-decked actuator (sensor) is larger extremely than horizontal deflection. Therefore, now we ignore all the effects of the horizontal deflection and membrane effects ; let applied force to the double-decked actuator (sensor) be zero ($f_3=0$ 、 $L_3(d_{31}, d_{32}, d_{36})=0$) and define the electrical and mechanical boundary conditions. Then we check the Table 8 to get $A_1=1$ 、 $A_2=0$ 、 $R_1=R_2= \infty$ 、 $\frac{1}{R_1} = \frac{1}{R_2} = 0$ 、 $d\alpha_1=dx$ 、 $d\alpha_2=0$, and the equation(3.19) can be simplified as follow :

$$L_3(u, v, w) = (\rho h \ddot{w}) \quad (I.15)$$

From [13], we get

$$L_3(u, v, w) = \frac{\partial}{\partial \alpha_1} \left\{ \frac{\partial}{\partial \alpha_1} \left[\left(D_{11} \left(\frac{\partial \beta_1}{\partial \alpha_1} + \frac{\beta_2}{A_1} \frac{\partial A_1}{\partial \alpha_2} \right) \right) \right] \right\} = (\rho h \ddot{w}) \quad (I.16)$$

where

$$\frac{\partial A_1}{\partial \alpha_2} \rightarrow 0 \quad (I.17)$$

And the above equation can be written another as follows.

$$\frac{\partial}{\partial \alpha_1} \left[\frac{\partial}{\partial \alpha_1} \left(\frac{u}{R_1} - \frac{1}{A_1} \frac{\partial w}{\partial \alpha_1} \right) \right] = (\rho h \ddot{w}) \quad (I.18)$$

where

$$\frac{u}{R_1} \rightarrow 0 \quad (I.19)$$

We can get simplified equation of motion;

$$D_{11} \frac{\partial^4 w}{\partial x^4} + \rho h \frac{\partial^2 w}{\partial t^2} = 0 \quad (I.20)$$

Bending stiffness is

$$D_{11} = \frac{1}{3} \left[c_{11} \left(\left(\frac{h}{2} \right)^3 - 0^3 \right) + c_{11} \left(0^3 - \left(-\frac{h}{2} \right)^3 \right) \right] = \frac{c_{11} h^3}{12} \quad (I.21)$$

Let the general solution of the vertical deflection be

$$w(x,t) = W(x)e^{j\omega t} ; \omega \text{ is frequency.}$$

Then the equation (I.20) becomes

$$\frac{\partial^4 W}{\partial x^4} + \lambda^4 W = 0 \quad (I.22)$$



where

$$\lambda^4 = \frac{\omega^2 \rho h}{D_{11}} \quad (I.23)$$

So that the general solution $w(x,t)$ is

$$w(x,t) = (c_1 \sin \lambda x + c_2 \cos \lambda x + c_3 \sinh \lambda x + c_4 \cosh \lambda x) e^{j\omega t} \quad (I.24)$$

We define electrical boundary conditions

$$\begin{cases} \psi_3|_{z=\pm h/2} = + V_3 e^{j\omega t} \\ \psi_3|_{z=0} = 0 \end{cases} \quad (\text{I.25})$$

Then define mechanical boundary conditions

$$w(x, t)|_{x=-L/2} = 0 \quad (\text{I.26})$$

$$\left. \frac{\partial w(x, t)}{\partial x} \right|_{x=-L/2} = 0 \quad (\text{I.27})$$

$$M(x, t)|_{x=+L/2} = 0 \quad (\text{I.28})$$

$$\left. \frac{\partial M(x, t)}{\partial x} \right|_{x=+L/2} = 0 \quad (\text{I.29})$$

Because

$$S_1 = \frac{\partial u}{\partial x} - z \frac{\partial^2 w}{\partial x^2} = d_{31} E_3 \quad (\text{I.30})$$

$$E_3 = -\frac{\partial \psi_3}{\partial z} = -\frac{6z}{h^2} V_3 e^{j\omega t} \quad (\text{I.31})$$

so that the equation (I.28) and equation (I.29) become

$$\left. \frac{\partial^2 w}{\partial x^2} \right|_{x=+L/2} = \frac{6d_{31}}{h^2} V_3 e^{j\omega t} \quad (\text{I.32})$$

$$\left. \frac{\partial^3 w}{\partial x^3} \right|_{x=+L/2} = 0 \quad (\text{I.33})$$

Then we can get the

$$c_1 = \frac{3d_{31} V_3 \sinh a}{(\cos a \cosh a - \sin a \sinh a) h^2 \lambda^2} \quad (\text{I.34})$$

$$c_2 = \frac{-3d_{31} V_3 \cosh a}{(\cos a \cosh a + \sin a \sinh a) h^2 \lambda^2} \quad (\text{I.35})$$

$$c_3 = \frac{3d_{31} V_3 \sin a}{(\cos a \cosh a + \sin a \sinh a) h^2 \lambda^2} \quad (\text{I.36})$$

$$c_4 = \frac{3d_{31} V_3 \cos a}{(\cos a \cosh a - \sin a \sinh a) h^2 \lambda^2} \quad (\text{I.37})$$

where

$$a = \frac{\lambda L}{2} \quad (\text{I.38})$$

Therefore we can get the general solution of the vertical deflection $w(x, t)$. Figure 3.2 shows the bending mode simulation and confirms the result. We apply $V=10$ volt on the driving electrode and can get bending result $w(x)|_{x=L/2} = 2.9 \times 10^{-9}$, that is confirmed by numerical solution by FEM.

Reference

- [1] Noboru Wakatsuki and Hiroshi Tanaka, "Finite Element Method Analysis of Single Crystal Tuning Fork Gyroscope for Suppression of its Inner Leakage Coupling," *Jpn. J. Appl. Phys.* Vol.36(1997) 3037-3040 Part 1, No. 5B, 30 May 1997.
- [2] Hiroshi Tanaka and Noboru Wakatsuki, "Electromechanical Coupling Coefficients for a New H-Type LiTaO₃ Piezoelectric Gyroscope," *Jpn. J. Appl. Phys.* Vol.37(1998) 2868-2871 Part 1, No. 5B, 30 May 1998.
- [3] Hideki Yokoyama, Subaru Kudo and Noboru Wakatsuki, "The Suppression of Mechanical Resonances of LiNbO₃ Actuator with Oppositely-Polarized Layers," *Jpn. J. Appl. Phys.* Vol.38(1999) 3334-3337 Part 1, No. 5B, 30 May 1999.
- [4] Mitsuharu Chiba and Noboru Wakatsuki, "Temperature Self-Compensated Lithium Tantalate Piezoelectric Gyroscope for Higher Stability," *Jpn. J. Appl. Phys.* Vol.39 (2000) 3069-3072 Part 1, No. 5B, 30 May 2000.
- [5] Keisuke Ono, Masanori Yachi¹ and Noboru Wakatsuki, "H-Type Single Crystal Piezoelectric Gyroscope of an Oppositely Polarized LiNbO₃ Plate," *Jpn. J. Appl. Phys.* Vol. 40 (2001) 3699-3703 Part 1, No. 5B, 30 May 2001.
- [6] Wakatuki, N.; Kudo, S.; Satoh, Y.; Tanaka, H, "A new approach to piezoelectric crystal gyroscopes for higher sensitivity," *Ultrasonics Symposium, 1998. Proceedings., 1998 IEEE , Volume: 1 , 5-8 Oct. 1998 Pages:477 - 480 vol.1.*
- [7] Chiba, M.; Wakatsuki, N., "experimental validation of temperature self-compensation for LiTaO₃ piezoelectric gyroscope," *Ultrasonics Symposium, 2000 IEEE, Volume: 1, 22-25 Oct. 2000 Pages: 883 - 888 vol.1.*
- [8] Sato, H.; Arai, F.; Ishihara, H.; Fukuda, T.; Iwata, H.; Itoigawa, K., "New PZT actuator using piezoelectric thin film on parallel plate structure," *Micromechatronics and Human Science, 1997. Proceedings of the 1997 International Symposium on , 5-8 Oct. 1997 Pages:79 – 84*
- [9] Yang, J.S.; Fang, H.Y.; Jiang, Q., "Analysis of a few piezoelectric gyroscopes," *Frequency Control Symposium and Exhibition, 2000. Proceedings of the 2000 IEEE/EIA International, 7-9 June 2000 Pages:79 – 86.*
- [10] Kudo, S.; Konno, M.; Sugawara, S.; Yoshida, T., "Consideration on equivalent mechanical circuits for vibratory gyroscope," *Ultrasonics Symposium, 1990. Proceedings., IEEE 1990 , 4-7 Dec. 1990 Pages:397 - 400 vol.1.*
- [11] Sherrit, S.; Wiederick, H.D.; Mukherjee, B.K., "Accurate equivalent circuits for unloaded piezoelectric resonators," *Ultrasonics Symposium, 1997. Proceedings., 1997 IEEE , Volume: 2 , 5-8 Oct. 1997 Pages:931 - 935 vol.2.*

- [12] Satoh, A.; Ohnishi, K.; Tourikawa, Y., "Characteristics of the piezoelectric vibratory gyrosensor constructed using a trident tuning-fork resonator," Ultrasonics Symposium, 1998. Proceedings., 1998 IEEE , Volume: 1 , 5-8 Oct. 1998 Pages:555 - 558 vol.1.
- [13] 周卓明, "壓電力學 Piezoelectricity Mechanics", 全華科技圖書股份有限公司, 民 92。
- [14] Sungsu Park, "Adaptive Control Strategies for MEMS Gyroscopes," UNIVERSITY OF CALIFORNIA, BERKELEY, Ph. D thesis, Fall 2000.
- [15] B.A.AULD, "AXOUSTIC FIELDS AND WAVES IN SOLIDS" VOLUME I, SECOND EDITION," professor (Research) of Applied Physics Stanford University, KRIEGER PUBLISHING COMPANY MALABAR, FLORIDA.
- [16] Wakatsuki, N.; Ono, M.; Yamada, S.; Takahashi, Y.; Kikuchi, K., "LiTaO₃ crystal fork vibratory gyroscope," Ultrasonics Symposium, 1994. Proceedings., 1994 IEEE , Volume: 1 , 1-4 Nov. 1994 Pages:581 - 584 vol.1
- [17] Wakatsuki, N.; Ono, M.; Yamada, S.; Kikuchi, K.; Yamauchi, M., "Suppression of null signals in LiTaO₃ crystal fork vibratory gyroscope," Ultrasonics Symposium, 1995. Proceedings., 1995 IEEE , Volume: 1,7-10 Nov. 1995 Pages:423 - 427 vol.1
- [18] M.Ono, N. Wakatsuki and Y.Takahashi: IEICE 79 (1996) 610.
- [19] ROY R. CRAIG, JR., "Mechanics of Materials," Second Edition, 2000 John Wiley & Sons
- [20] D. Boucher, M. Lagier, and C. Maerfeld. "Computation of the Vibration Modes for Piezoelectric Array Transducers Using a Mixed Finite Element Perturbation Method". IEEE Trans. Sonics and Ultrasonics, Vol. SU-28, No. 5. 1981.
- [21] 池田拓郎 著、陳世春 譯著, "基本壓電材料學", 復漢出版社出版(1985)
- [22] Philip W. Loveday and Craig A. Rogers, "Modification of Piezoelectric Vibratory Gyroscope Resonator Parameters by Feedback Control," IEEE TRANSACTIONCS, FERROELECTRICS, AND FREQUENCY CONTROL, VOL. 45, NO 5, SEPTEMBER 1998.
- [23] A. M. Shkel, R. Horowitz, A. A. Seshia, S. Park, R. T. Howe, "Dynamics and Control of Micromachined Gyroscopes," Proc. Amer. Contr. Conf., San Diego, CA, June 1999, pp. 2119-2124, 1999.
- [24] R. P. Leland, "Lyapunov Based Adaptive Control of a MEMS Gyroscope," Proc. 2002 American Control Conf., Anchorage, AK, p. 3765-3770, 2002.
- [25] Robert P. Leland and Yacov Lipkin, Alton Highsmith, "Adaptive Oscillator Control for a Vibrational Gyroscope," University of Alabama Tuscaloosa, AL
- [26] Thomas B. Gabrielson, "Micromachined Mechanical-Thermal Noise inAcoustic and Vibration sensors," IEEE TRANSACTIONS ON ELECTRON DEVICES,

VOL. 40, NO. 5. MAY 1993

- [27] R. P. Leland , “Mechanical-Thermal Noise in Vibrational Gyroscopes,”
Proceedings of the American Control Conference Arlington, VA June 25-27,
2001
- [28] Felix A. Levinzon, “Fundamental Noise Limit of Piezoelectric Accelerometer,”
IEEE SENSORS JOURNAL, VOL. 4, NO. 1, FEBRUARY 2004
- [29] Stephen D. Senturia, “Microsystem Design,” 2001 Kluwer Academic Publishers
- [30] Chris C. Painter and Andrei M. Shkel, “Active Structural Error Suppression in
MEMS Vibratory Rate Integrating Gyroscopes,” IEEE SENSORS JOURNAL,
VOL. 3, NO 5, OCTOBER 2003.



Table 1 Electromechanical Coupling Coefficients for Driving and Detecting Electrodes (fork type) [2]

	Resonance frequency : f_0	k^2 of driving electrode	k^2 of detecting electrode
f_x mode	18.6203(kHz)	0.00584	1.07×10^{-5}
f_y mode	20.6933(kHz)	8.7×10^{-5}	0.00389

Table 2 Electromechanical Coupling Coefficients for Symmetrical Electrode [2]

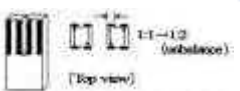
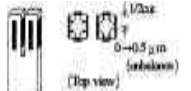
	Driving electrode				Detecting electrode			
	Balanced		Unbalanced		Balanced		Unbalanced	
	f_0 (kHz)	k^2	f_0 (kHz)	k^2	f_0 (kHz)	k^2	f_0 (kHz)	k^2
fx mode	18.6207	0.0121	18.6204	0.0099	18.6859	0	18.6301	21.5ppm
fz mode	20.7915	0	20.7901	9.6ppm	20.6782	0.0048	20.6731	0.0066
Configur- -ation of electrode								

Table 3 The properties of the four piezoelectric state variables

T	6 x 1	$\frac{N}{m^2}$	stress components
S	6 x 1	$\frac{m}{m}$	strain components
E	3 x 1	$\frac{N}{C}$	electric field components
D	3 x 1	$\frac{C}{m^2}$	electric charge density displacement components

Table 4 The matrix properties of the different forms

s	6 x 6	$\frac{m^2}{N}$	compliance coefficients
c	6 x 6	$\frac{N}{m^2}$	stiffness coefficients
ε	3 x 3	$\frac{F}{m}$	electric permittivity
d	3 x 6	$\frac{C}{N}$	piezoelectric coupling coefficients for d form
e	3 x 6	$\frac{C}{m^2}$	piezoelectric coupling coefficients for e form
g	3 x 6	$\frac{m^2}{C}$	piezoelectric coupling coefficients for g form
h	3 x 6	$\frac{N}{C}$	piezoelectric coupling coefficients for h form

Table 5 Compliance Constants of LiTaO₃

Compliance Constants s_{ij} ($10^{-12} \text{ m}^2 / \text{newton}$)	
s_{11}	4.87
s_{22}	—
s_{33}	4.36
s_{44}	10.8
s_{55}	—
s_{66}	—
s_{12}	-0.58
s_{13}	-1.25
s_{14}	0.64
s_{16}	—
s_{23}	—
s_{25}	—

**Table 6 Piezoelectric Strain Constants of LiTaO₃**

Piezoelectric Strain Constants d_{ij} ($10^{-12} \text{ coulomb} / \text{newton}$)	
d_{11}	20.3
d_{14}	—
d_{15}	24.5
d_{22}	6.0
d_{25}	—
d_{31}	—
d_{32}	5.3
d_{33}	7.5
d_{36}	0.9

Table 7 Permittivity Strain Constants of LiTaO₃

Piezoelectric Strain Constants d_{ij} (10^{-12} coulomb/newton)	
$\varepsilon_{11} / \varepsilon_0$	41
$\varepsilon_{22} / \varepsilon_0$	—
$\varepsilon_{33} / \varepsilon_0$	43

$$\dagger \varepsilon_0 = 8.854 \times 10^{-12} \text{ farads/m}$$

Table 8 Stiffness Constants of LiTaO₃

Stiffness Constants c_{ij} (10^{10} newton/m ²)	
c_{11}	23.3
c_{22}	—
c_{33}	27.5
c_{44}	9.4
c_{55}	—
c_{66}	—
c_{12}	4.7
c_{13}	8.0
c_{14}	-1.1
c_{16}	—
c_{23}	—
c_{25}	—

Table 9 Crystal Symmetry Class and Mass Density

Material	Lithium Tantalate
Chemical Formula	LiTaO ₃
Symmetry Class	Trig. 3m
Density (kg/m ³)	7450

Table 10 Power Spectral Density of Noise

Power spectral density of noise	
PSD of mechanical noise	$2.62 \times 10^{-12} \text{ N}/\sqrt{\text{Hz}}$
PSD of electrical noise	$2.12 \times 10^{-8} \text{ V}/\sqrt{\text{Hz}}$
Position noise of mechanical noise	$5.27 \times 10^{-12} \text{ V}$
Position noise of electrical noise	$3.59 \times 10^{-8} \text{ V}$
Velocity noise of mechanical noise	$1.16 \times 10^{-6} \text{ V}$
Position noise of electrical noise	$7.9 \times 10^{-3} \text{ V}$

Table 11 Parameters of the designed H-gyro

Parameters of Approximated 2 nd Order Model	
mass	3.036×10^{-8} kg
Resonant frequency of Y mode	215 kHz
Resonant frequency of H mode	220 kHz
Q-value	100

Table 12 Parameters of Approximated 2nd Order Model

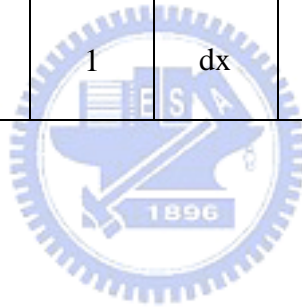
Parameters of Approximated 2 nd Order Model	
D_{xx}	13509
D_{yy}	13823
D_{xy}	11
K_{xx}	1350900^2
K_{yy}	1382300^2
K_{xy}	801796040
Ω (rad/s)	0.33

Table 13 Selected Adaptive Control Gains

Selected adaptive control gains	
γ_D	100
γ_R	100
γ_Ω	150
γ_1	100
γ_2	100

Table 14 Parameters of Different Configurations

Configuration	A_1	A_2	$d\alpha_1$	$d\alpha_2$	R_1	R_2
Ring	1	1	dx	$Rd\theta$	R	∞
Beam	1	0	dx	0	∞	∞
Radial shell	1	R	dx	$d\theta$	∞	R
Disk	1	R	dr	$d\theta$	∞	∞
Tetragon plane	1	1	dx	dy	∞	∞



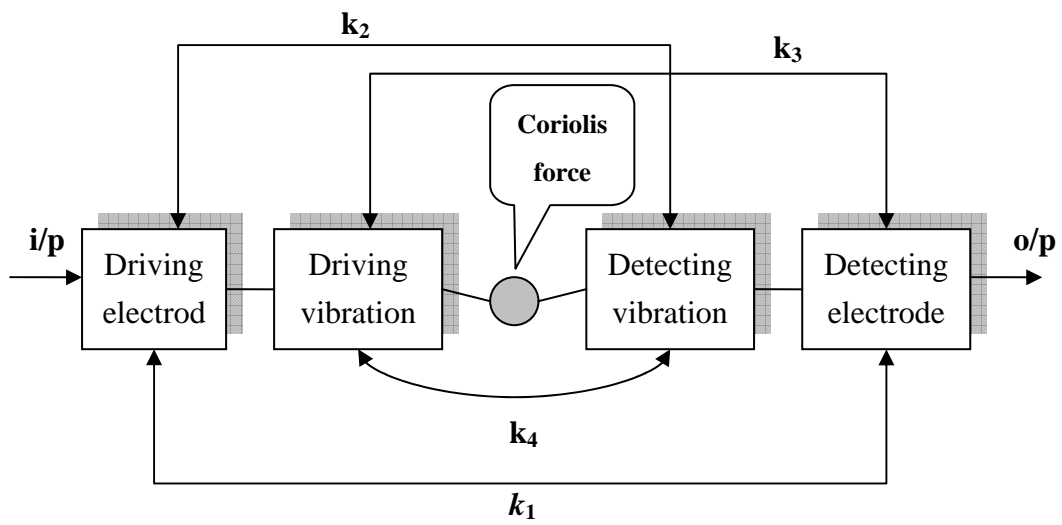


Figure 1.1 Coupling classifications of gyroscope

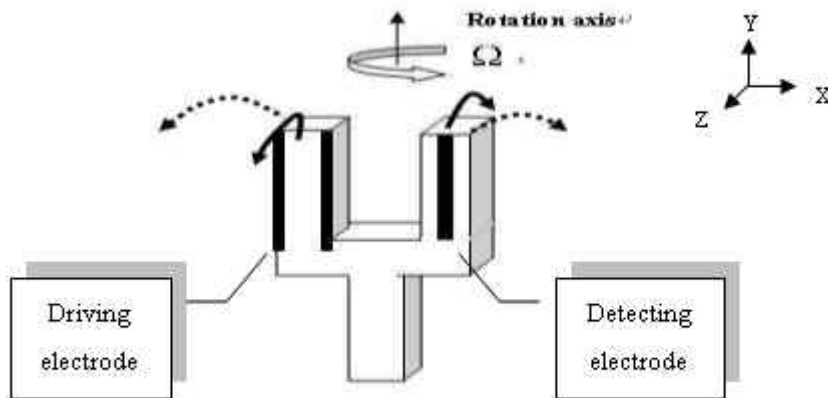


Figure 1.2 Conventional fork type piezoelectric gyroscope

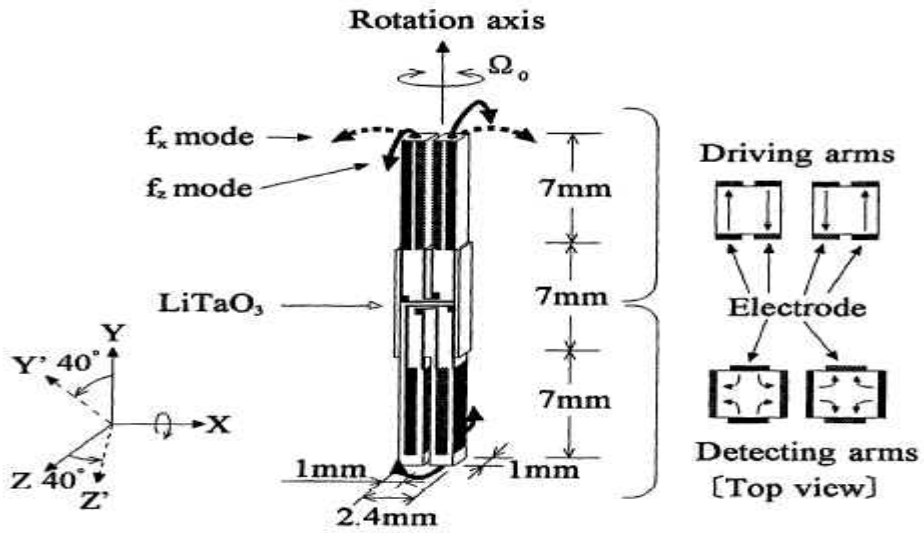


Figure 1.3 H-type LT piezoelectric gyroscope [2]

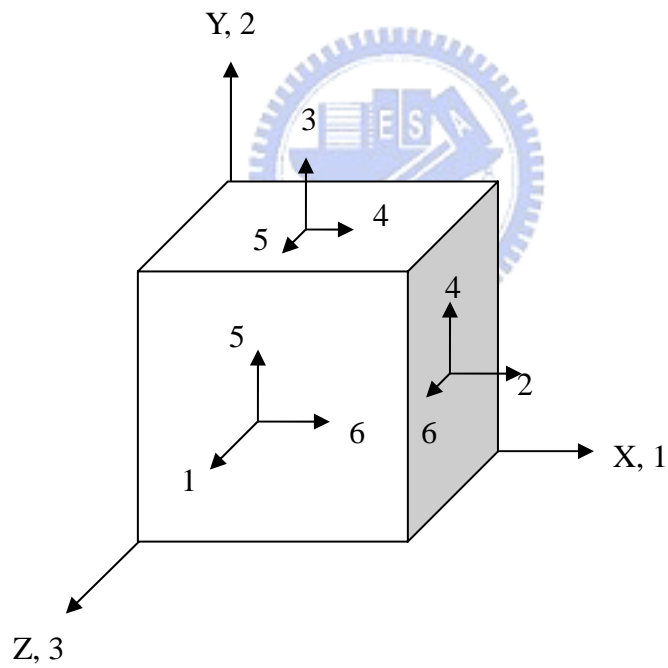


Figure 2.1 Inertia coordinate of the piezoelectric material

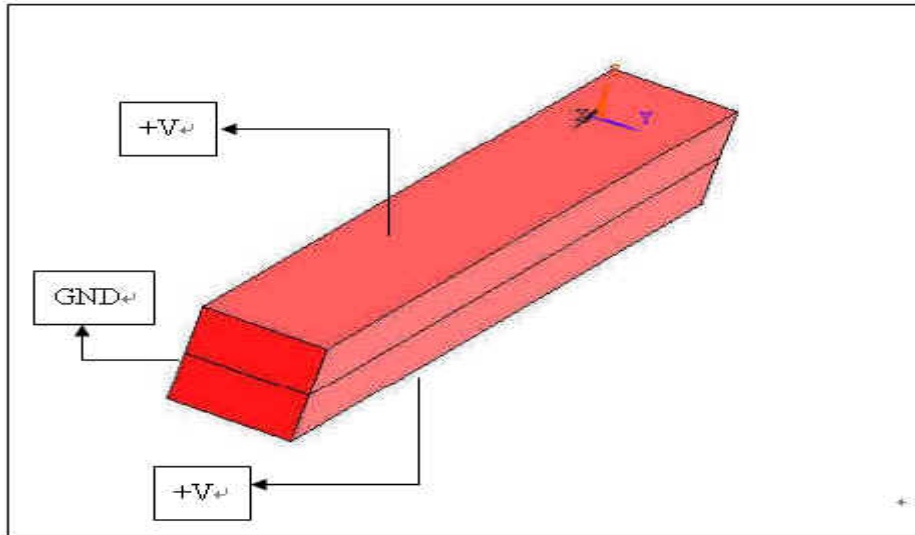


Figure 3.1 bending model concept.

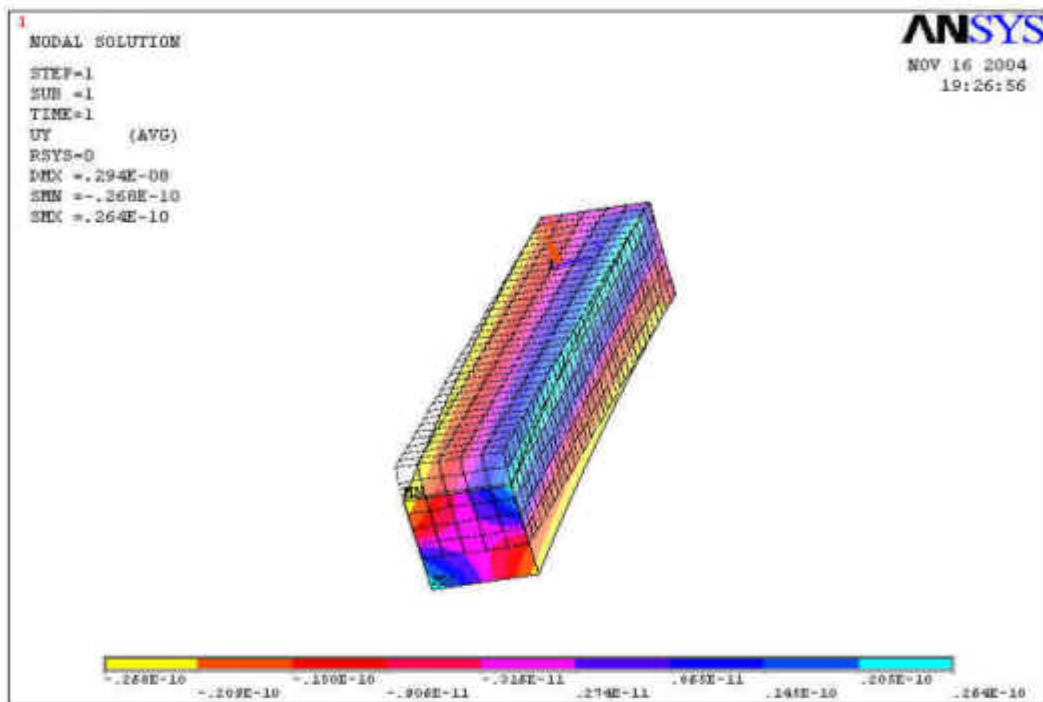


Figure 3.2 Bending mode simulation by ANSYS

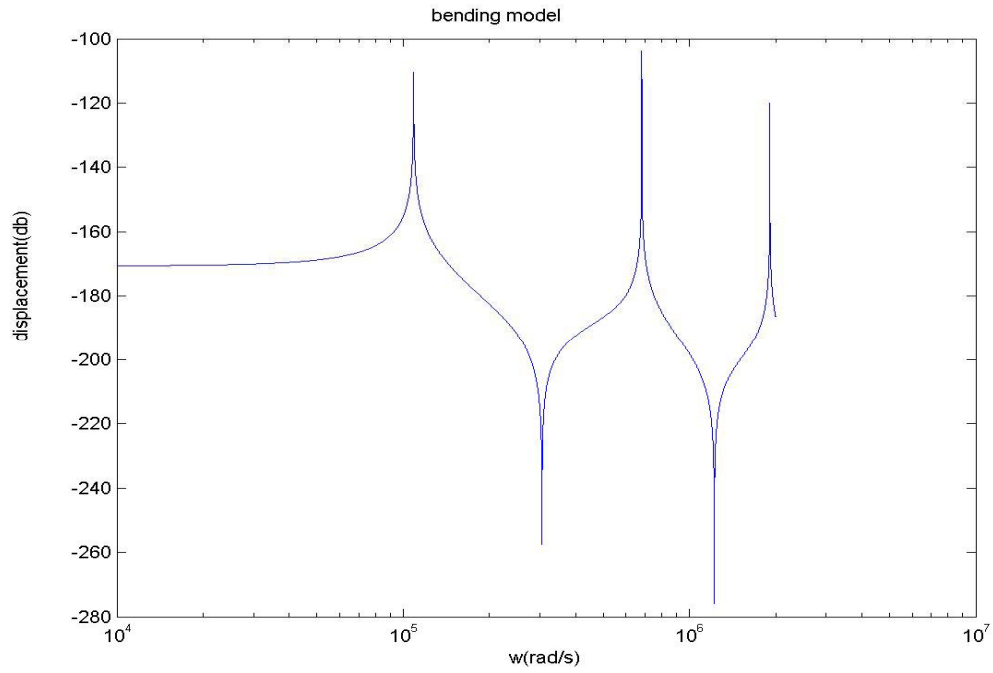


Figure 3.3 Displacement vs. frequency of bending mode

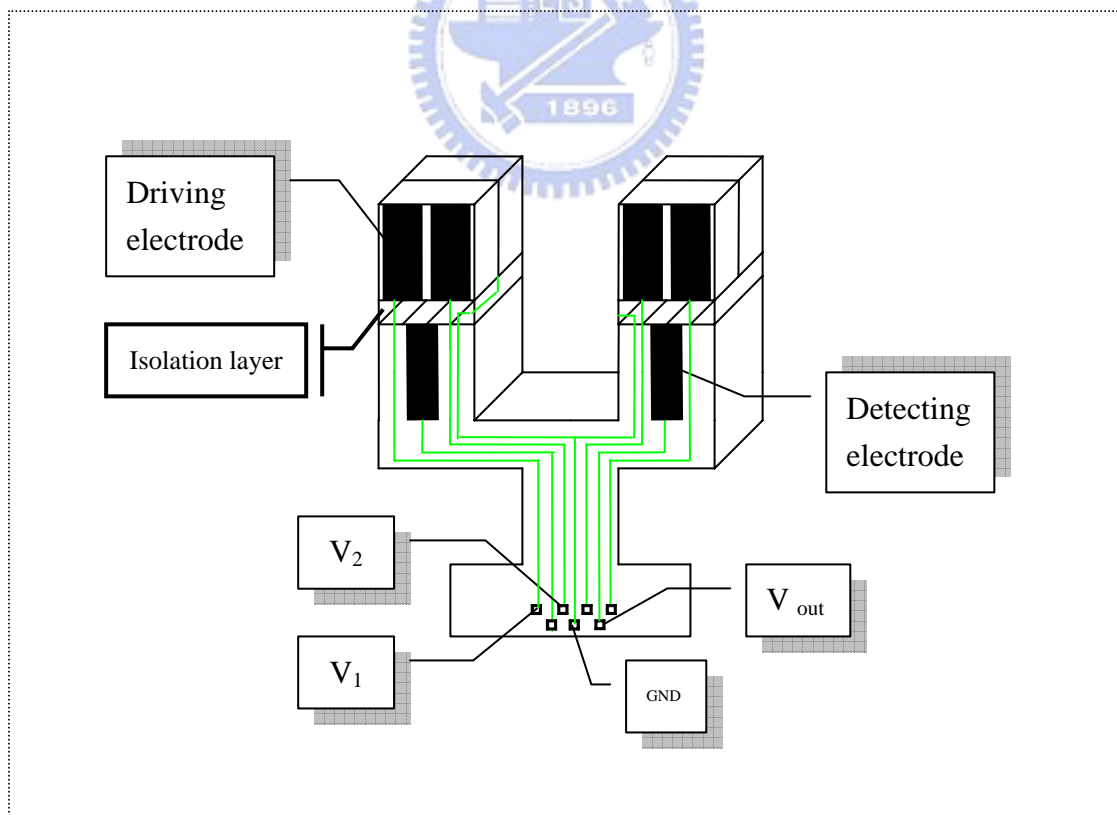


Figure 3.4 The designed gyroscope (case I)

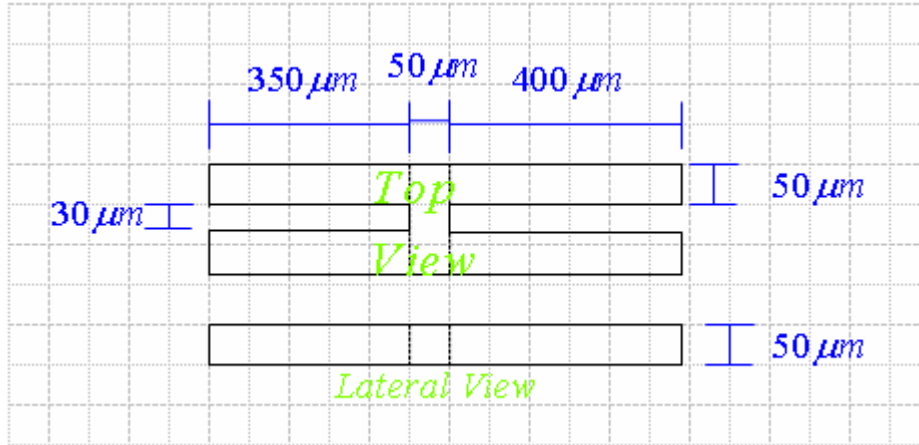


Figure 3.5 Size of the designed gyroscope model

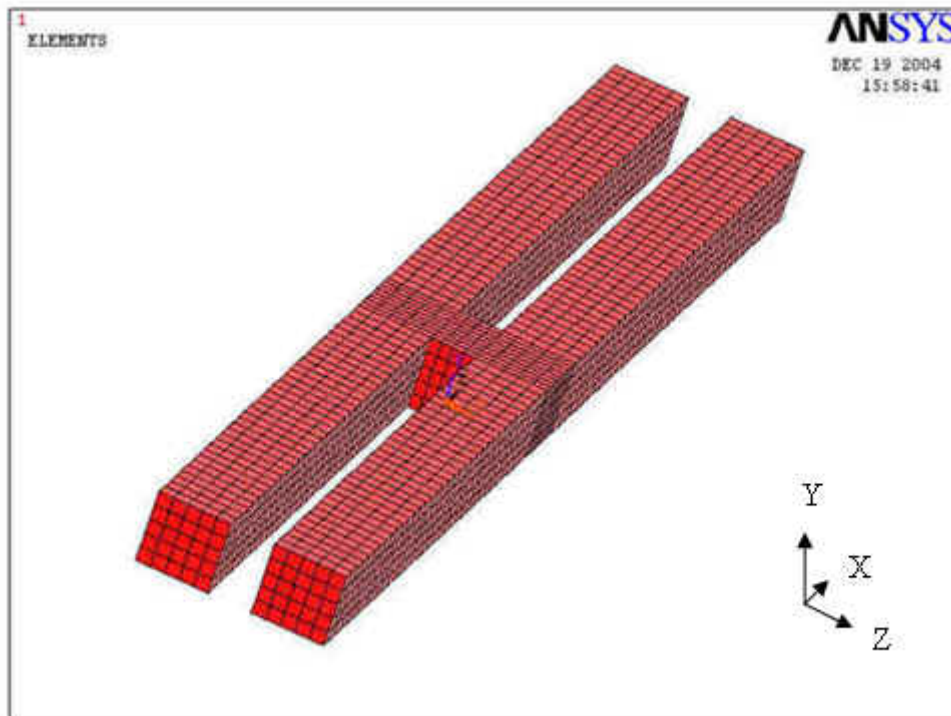


Figure 3.6 Configuration of gyroscope model (case II)

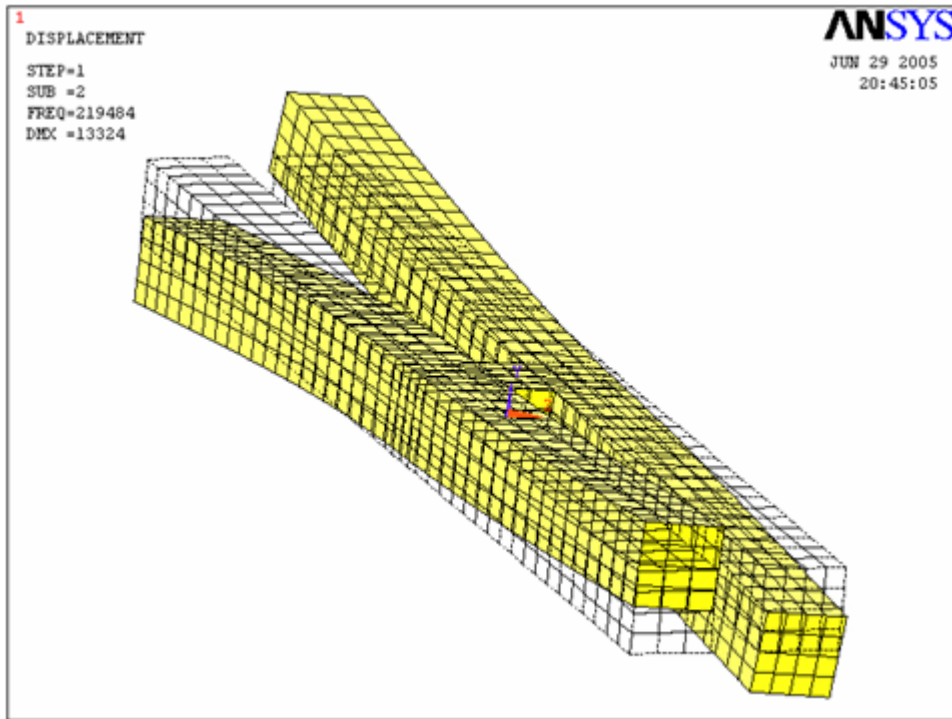


Figure 3.7 Modal analysis of the designed model by ANSYS (H mode)

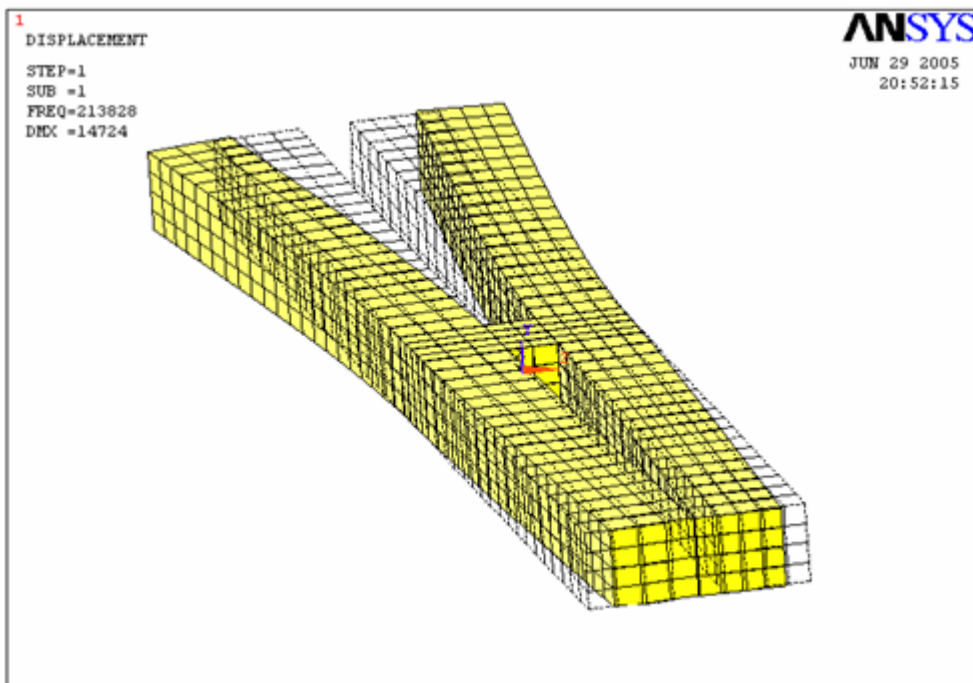


Figure 3.8 Modal analysis of the designed model by ANSYS (Y mode)

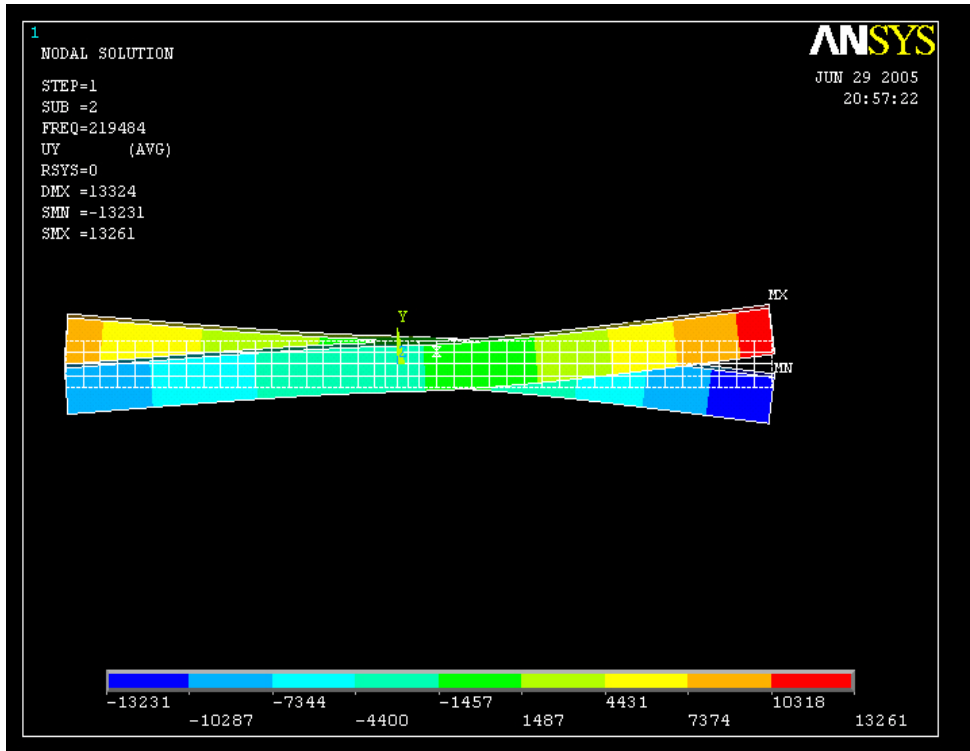


Figure 3.9 Lateral view of the designed model by ANSYS (H mode)

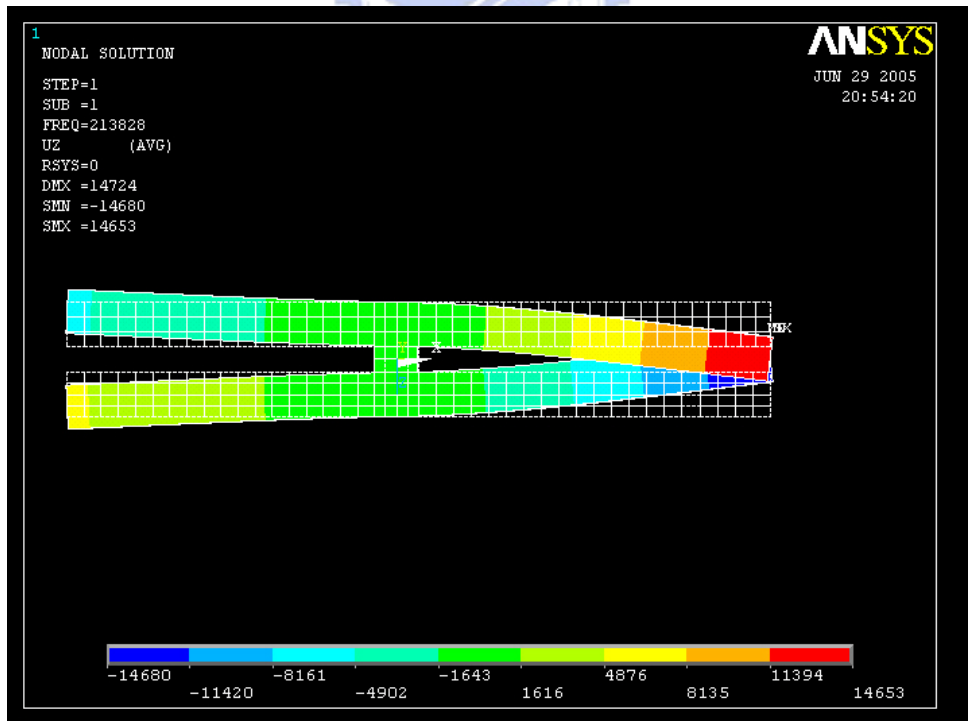


Figure 3.10 Lateral view of the designed model by ANSYS (Y mode)

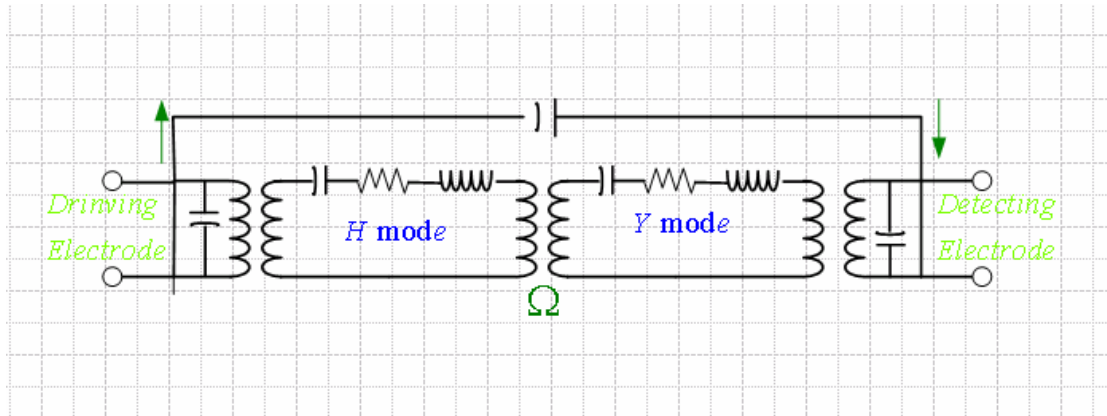


Figure 3.11 Schema of equivalent circuit between driving and detection electrodes

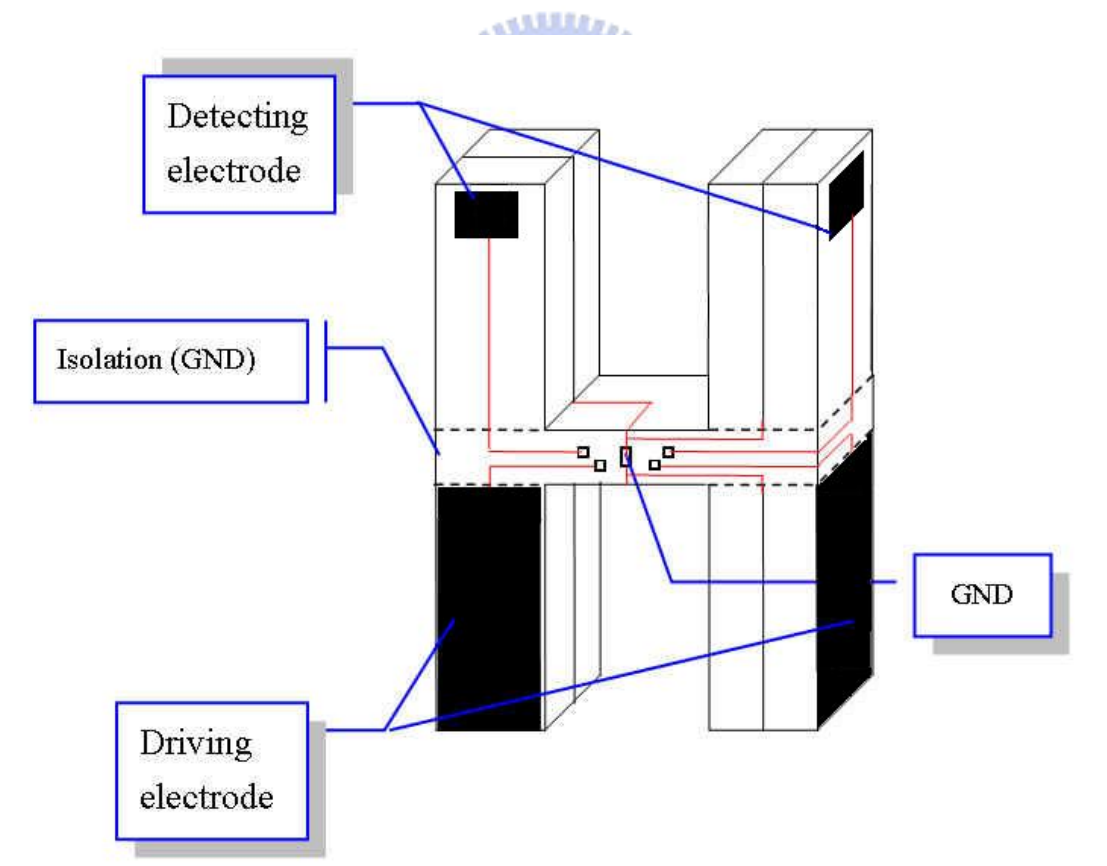


Figure 3.12 Configuration of the designed model by ANSYS

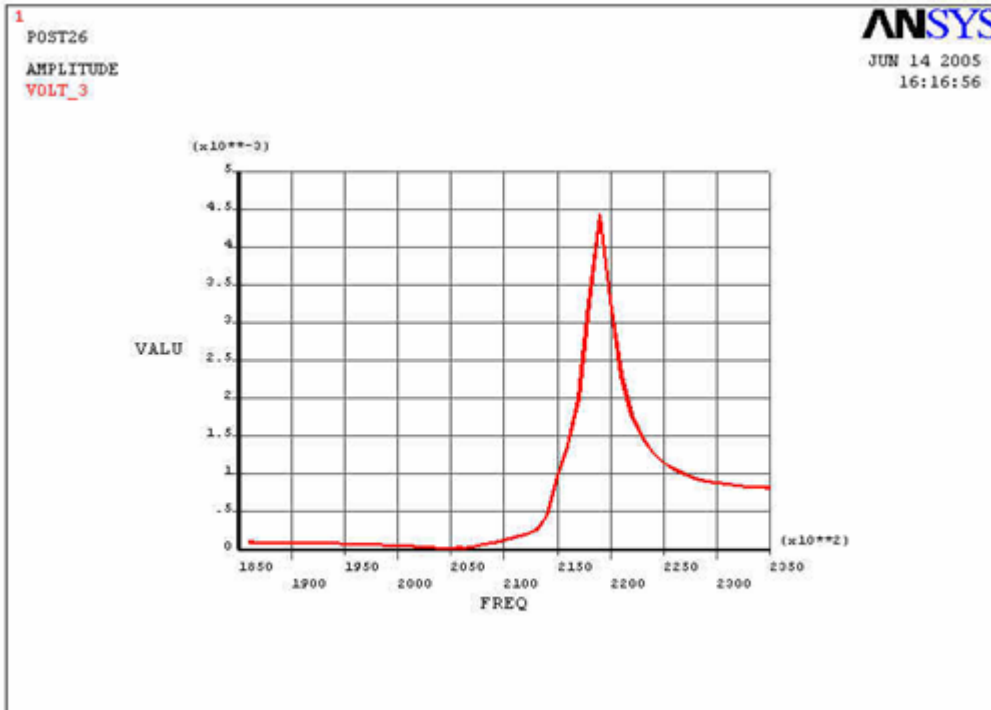


Figure 3.13 Frequency response with intermediate isolation

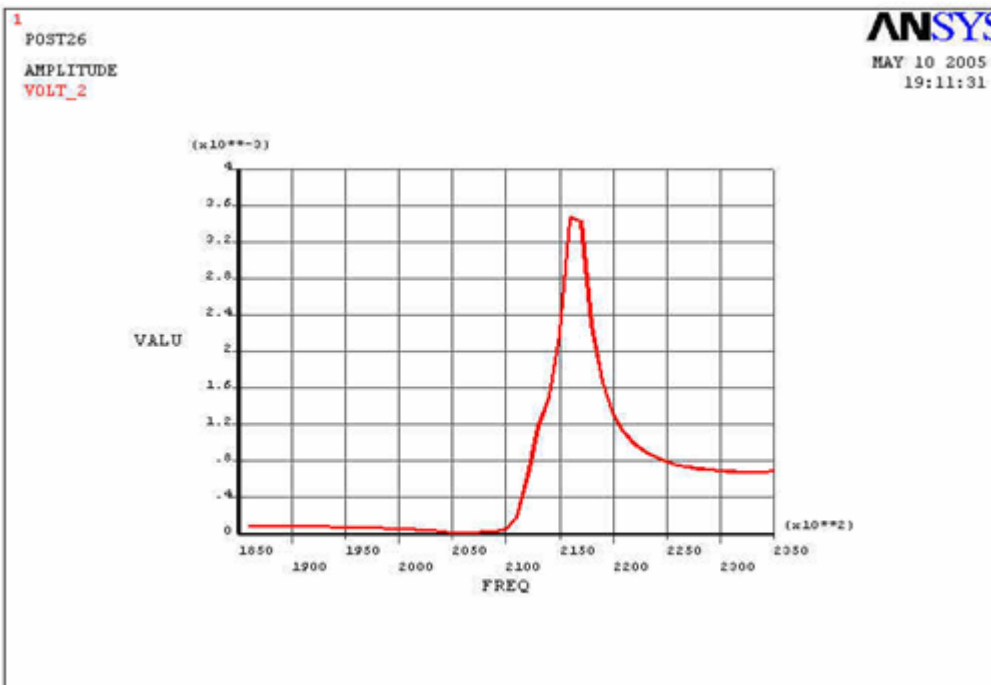


Figure 3.14 Frequency response without any intermediate limit

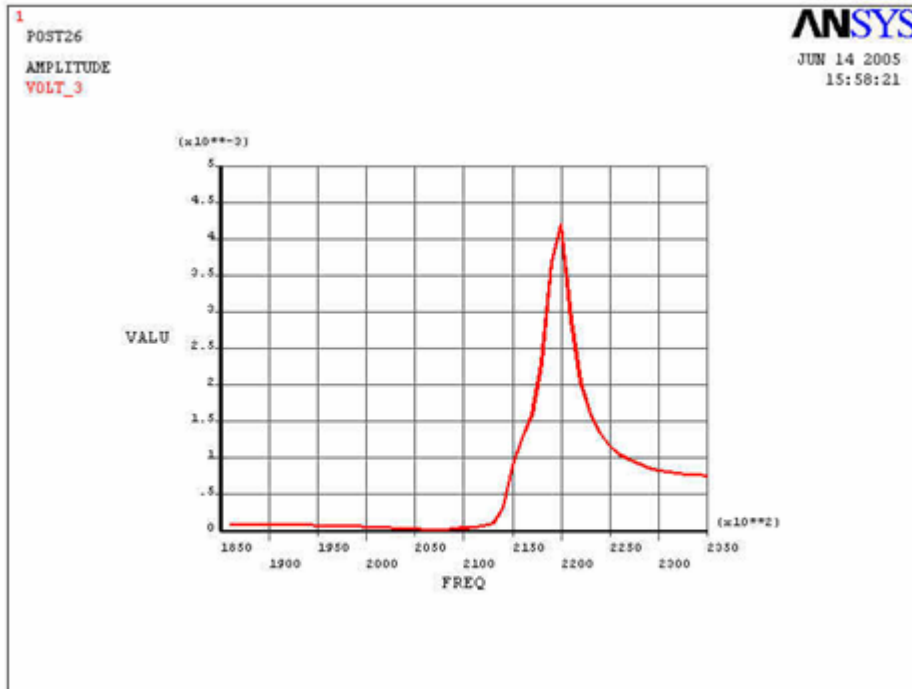


Figure 3.15 Frequency response with intermediate planar electrode GND

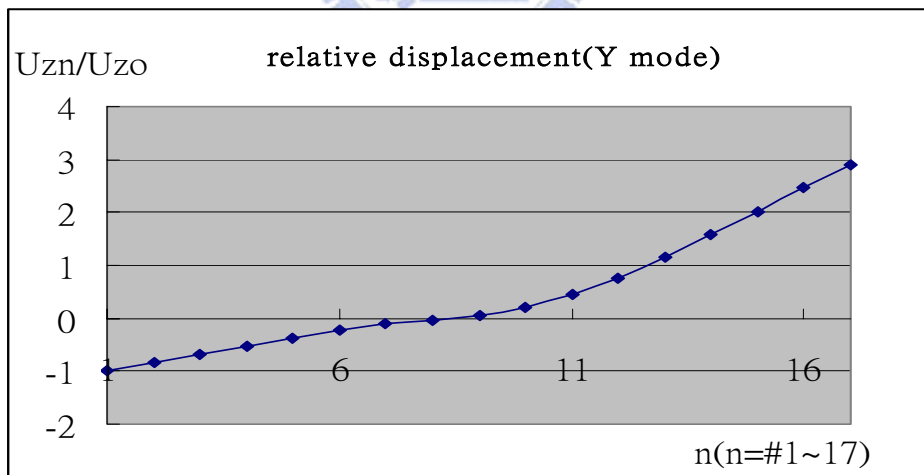


Figure 3.16 Relative displacements of the designed model (Y mode)

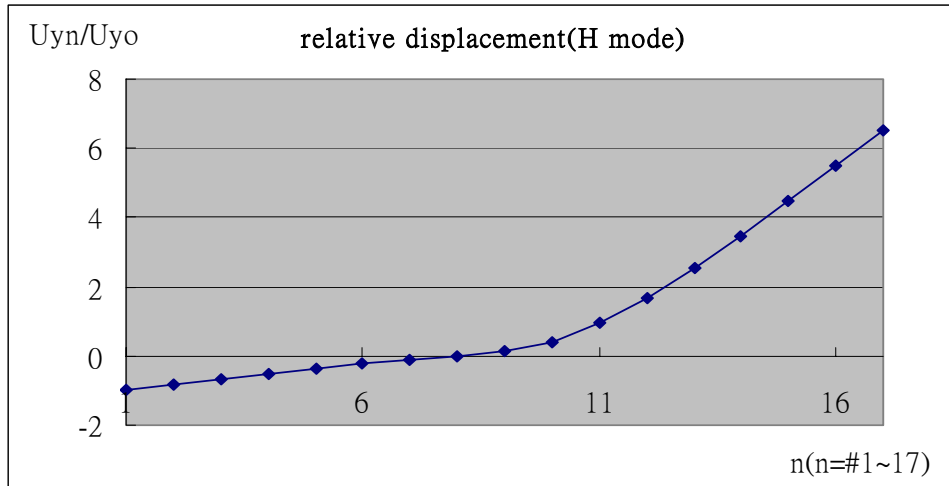


Figure 3.17 Relative displacements of the designed model (H mode)

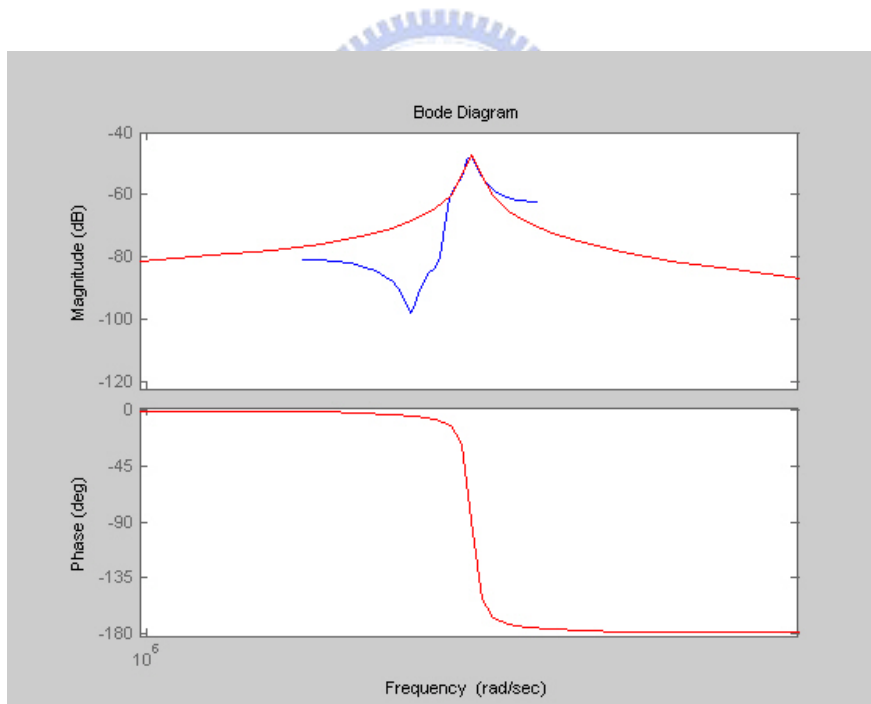


Figure 3.18 Curve fitting of frequency response (H mode)

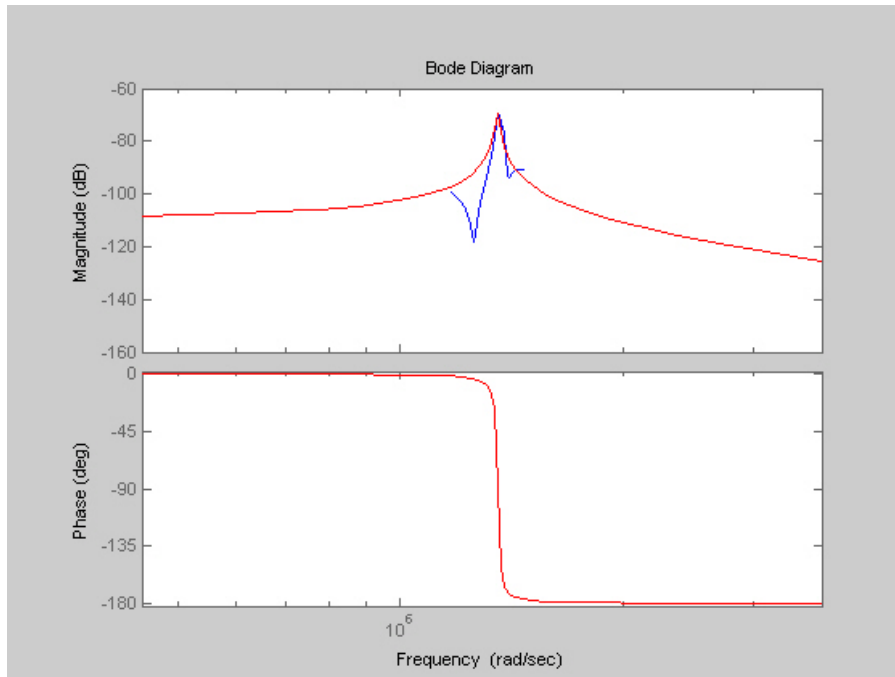


Figure 3.19 Curve fitting of frequency response (Y mode)

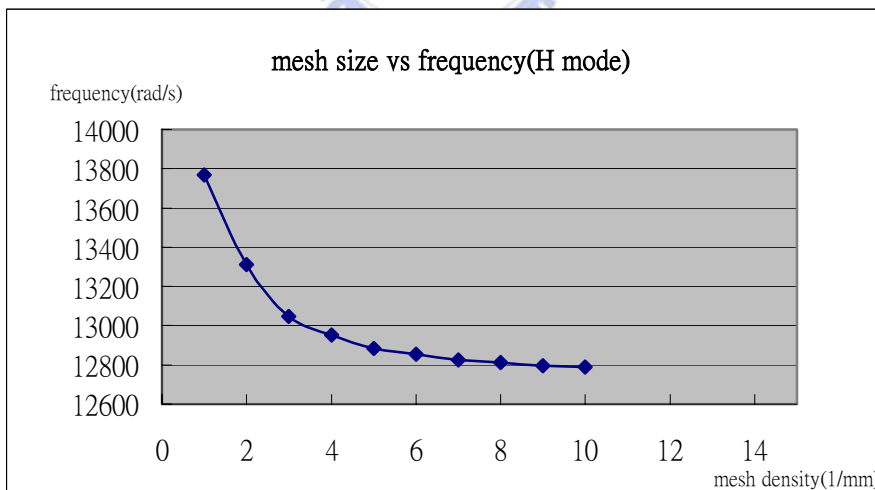
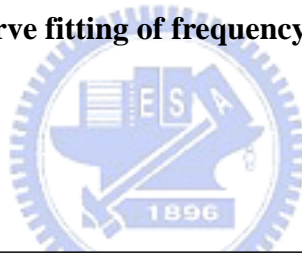


Figure 3.20 Convergence analysis (H mode)

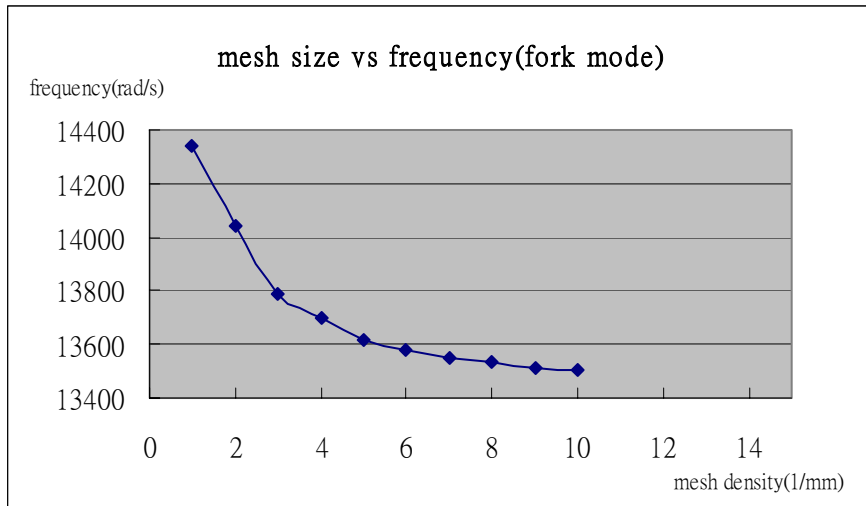


Figure 3.21 Convergence analysis (fork mode)

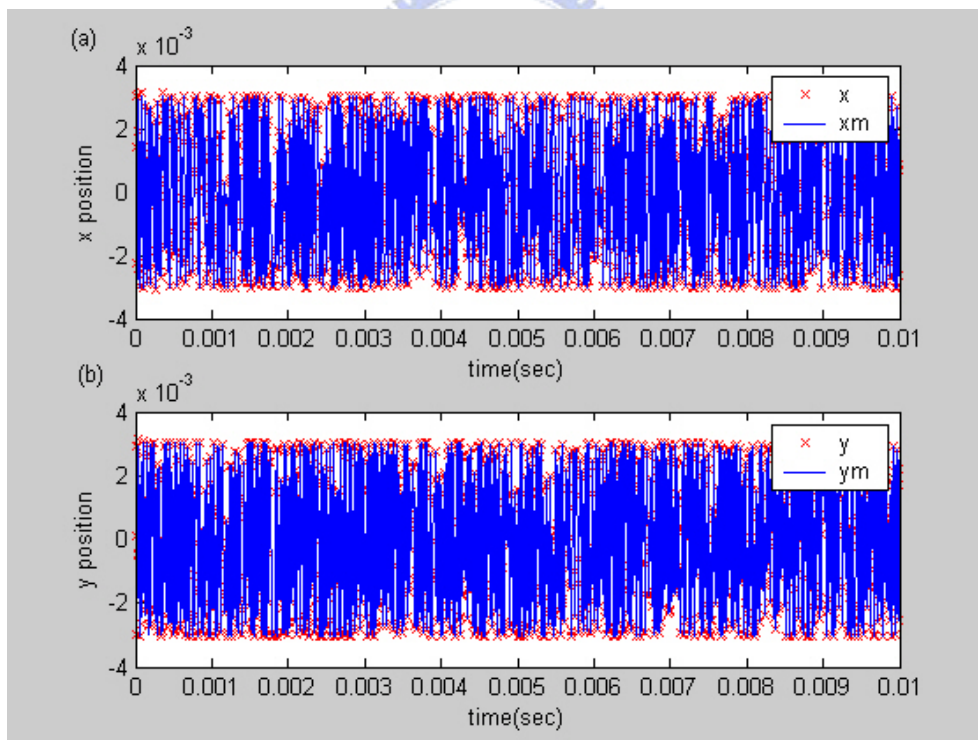


Figure 4.1 Trajectories of x and y axes (a) tracking signal of x axis. (b) tracking signals of y axis.

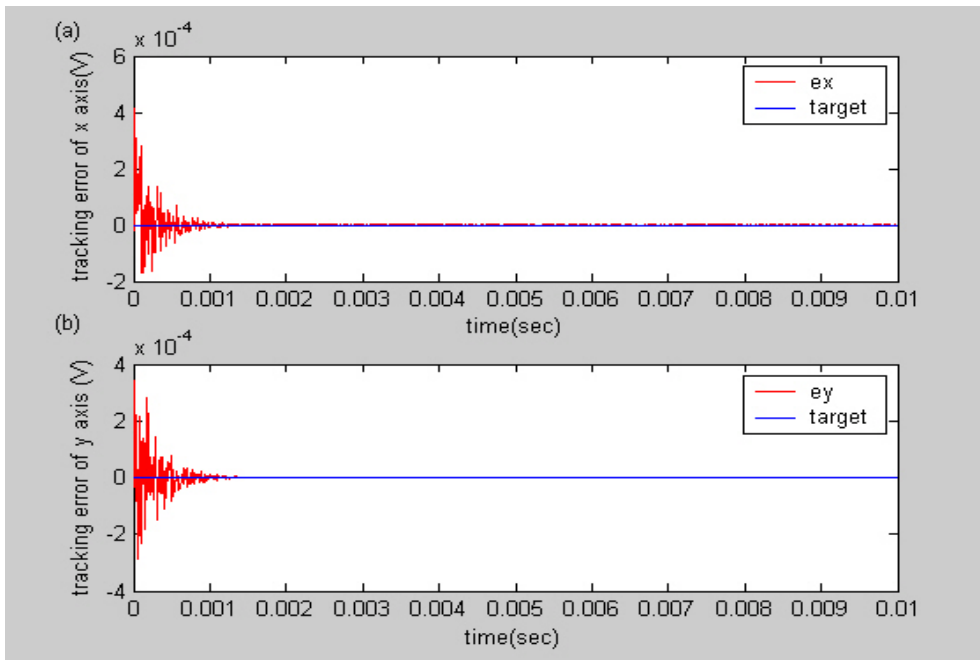


Figure 4.2 (a) tracking error of x axis. (b) tracking error of y axis.

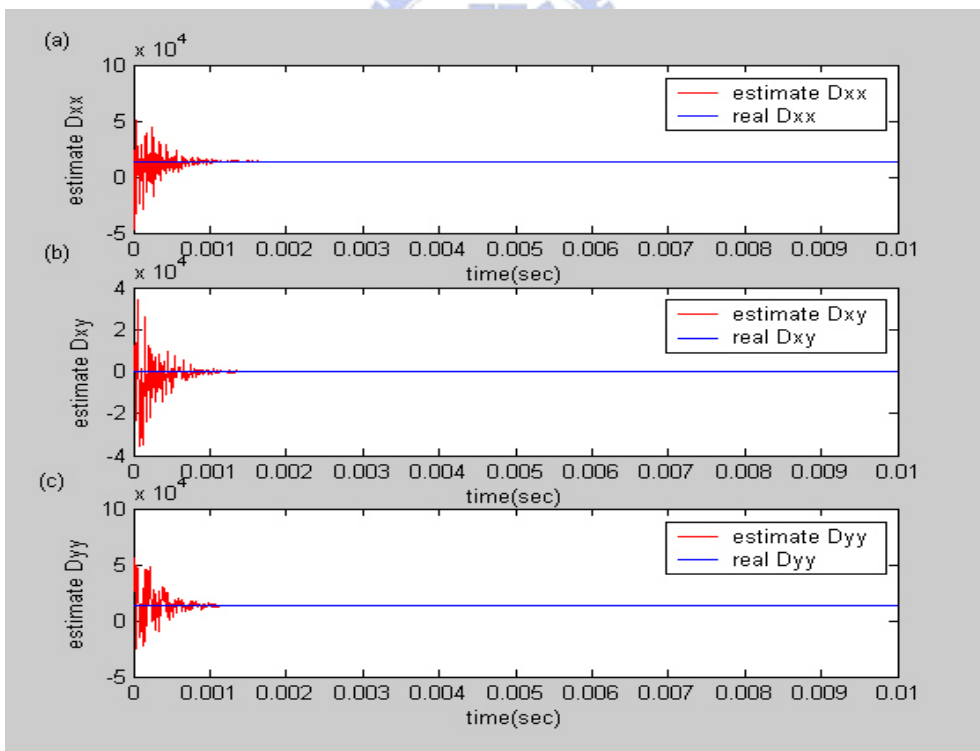


Figure 4.3 Estimations of damping terms. (a)estimation of D_{xx} . (b)estimation of D_{xy} . (c)estimation of D_{yy} .

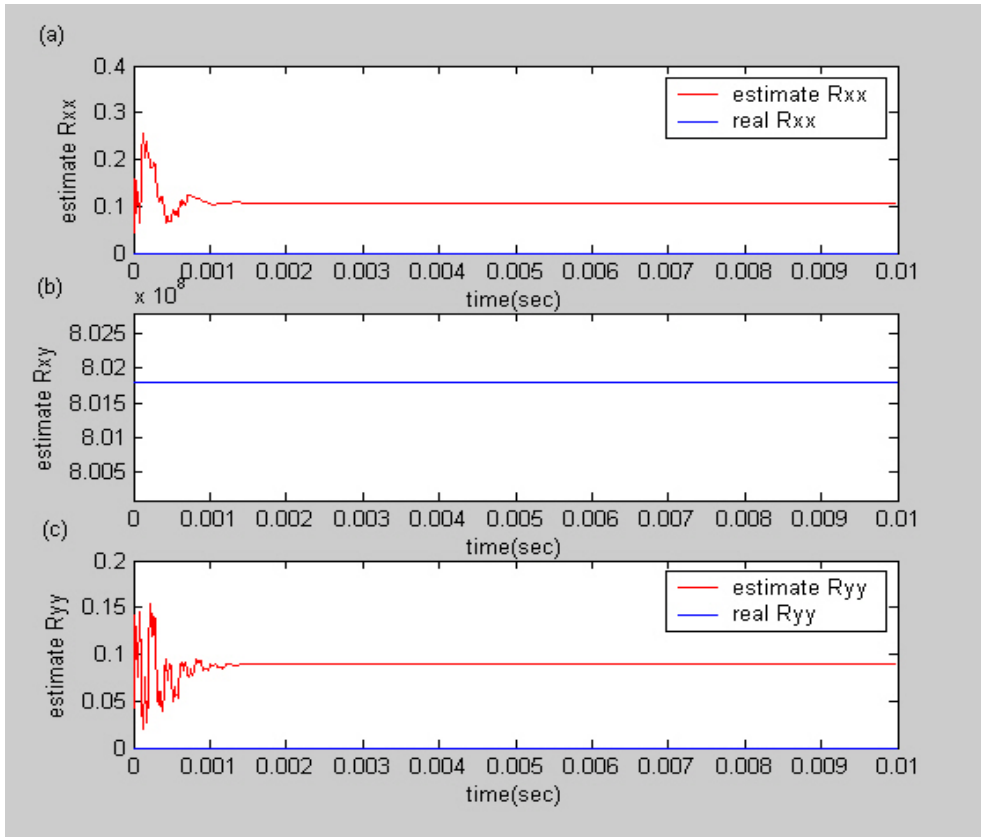


Figure 4.4 Estimations of R terms. (a)estimation of R_{xx} . (b)estimation of R_{xy} . (c)estimation of R_{yy} .

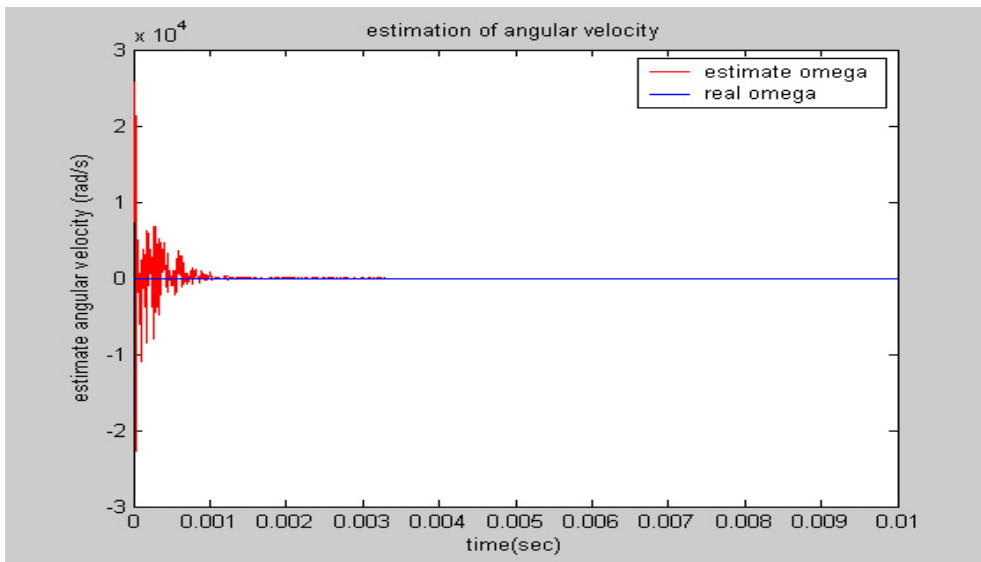


Figure 4.5 Estimation of angular velocity.

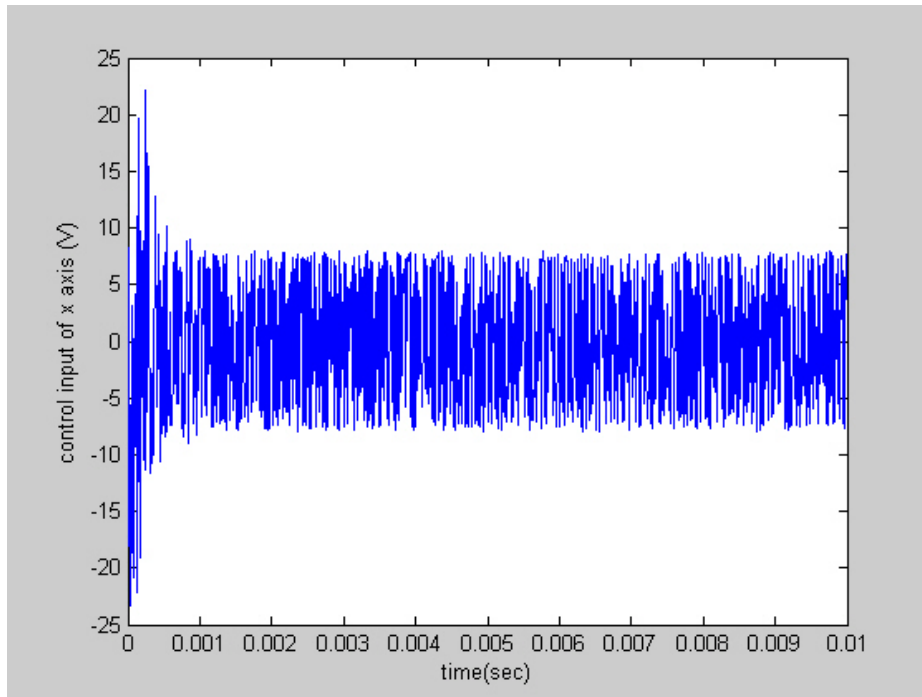


Figure 4.6 Control input of x axis.

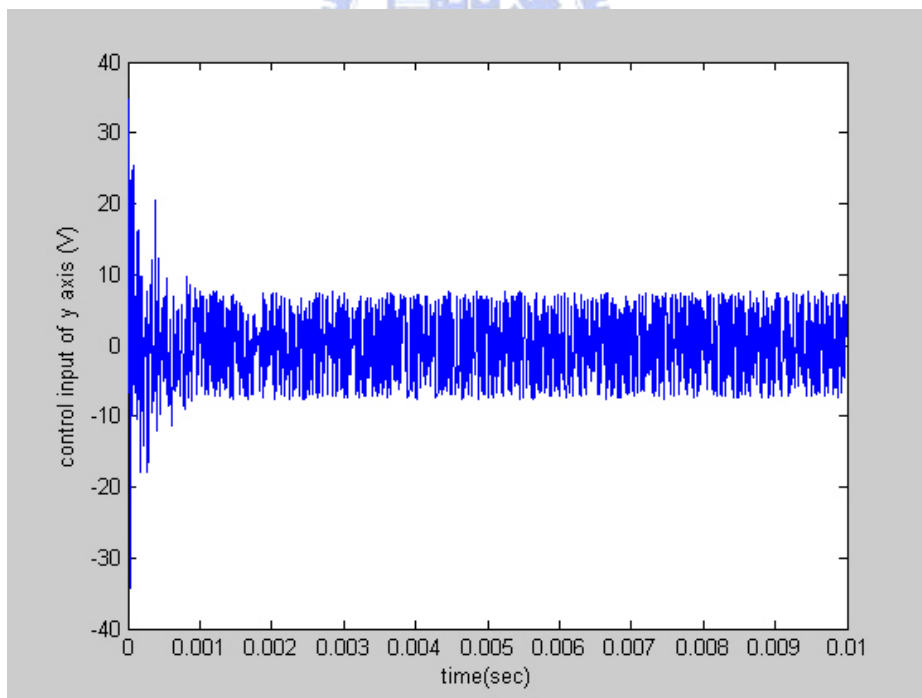


Figure 4.7 Control input of y axis.

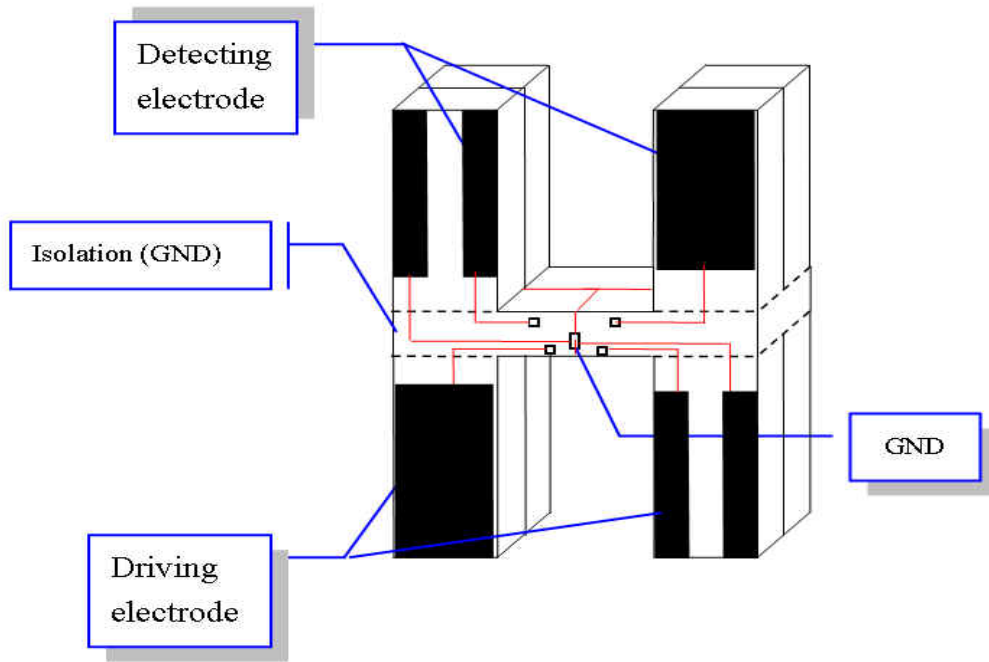


Figure 5.1 Planar electrode design of H-gyro.

